

A skin-integrated multimodal haptic interface for immersive tactile feedback

Received: 31 January 2023

Accepted: 20 October 2023

Published online: 30 November 2023

 Check for updates

Ya Huang ^{1,2,15}, Jingkun Zhou ^{1,2,15}, Pingchuan Ke ^{3,4,15}, Xu Guo^{5,6,15}, Chun Ki Yiu^{1,2}, Kuanming Yao ¹, Shaoyu Cai^{4,7}, Dengfeng Li ^{1,2}, Yu Zhou ⁸, Jian Li ^{1,2}, Tsz Hung Wong¹, Yiming Liu ¹, Lei Li ⁹, Yuyu Gao¹, Xingcan Huang ¹, Hu Li¹, Jiyu Li^{1,2}, Binbin Zhang^{1,2}, Zhenlin Chen^{1,2}, Huanxi Zheng¹⁰, Xingyu Yang⁴, Haichen Gao⁴, Zichen Zhao ^{5,6}, Xu Guo^{5,6}, Enming Song¹¹, Hui Wu ¹², Zuankai Wang ¹⁰, Zhaoqian Xie ^{5,6,13}✉, Kening Zhu ^{4,14}✉ & Xinge Yu ^{1,2,14}✉

Haptic feedback can be used to improve immersion in virtual and augmented reality systems. However, wearable haptic devices typically provide limited feedback, such as simple vibration, and are restricted to a narrow bandwidth of tuneable frequency or to single tactile perceptions. Here, we report a skin-integrated wireless haptic interface that is based on actuator arrays and offers multimodal and complex feedback mechanisms. Different feedback modes—mechanical, electrotactile and thermal—in the interface are used to selectively activate different cutaneous receptors, providing users with diverse haptic sensations. The selective stimulating mechanism is inspired by the neural tactile sensing system and can reproduce tactile information of fine roughness, macro roughness, slipperiness, force and temperature.

Tactile sensations involve the acquisition of complex and coupled data via mechanoreceptors in the skin, and are difficult to accurately reproduce using haptic feedback interfaces^{1–3}. Various hardware approaches for haptic feedback have been explored, including grounded devices⁴, active surfaces⁵, joysticks⁶ and wearable devices³. Wearable devices offer the highest mobility and potential for interaction with the real world (Supplementary Fig. 1)^{3,7}. In addition, devices that form a conformal contact with the skin can minimize the impact

on physical interaction and offer an efficient information transmission path between users and devices^{7,8}. However, skin-integrated haptic interfaces are still in the early stages of development⁹.

Tactile perception can be classified into two main subsystems: one for temperature, detected by free nerve endings and Krause end bulbs in the skin; and one for mechanical stimuli, detected by Meissner's corpuscles, Merkel's discs, Pacinian corpuscle and Ruffini endings (Fig. 1a)^{10–12}. Tactile sensation is associated with multidimensional factors, including

¹Department of Biomedical Engineering, City University of Hong Kong, Hong Kong, China. ²Hong Kong Centre for Cerebro-Cardiovascular Health Engineering, Hong Kong Science Park, Hong Kong, China. ³Department of Sociology, Hong Kong Shue Yan University, Hong Kong, China. ⁴School of Creative Media, City University of Hong Kong, Hong Kong, China. ⁵State Key Laboratory of Structural Analysis, Optimization and CAE Software for Industrial Equipment, Dalian University of Technology, Dalian, China. ⁶Department of Engineering Mechanics, Dalian University of Technology, Dalian, China. ⁷Engineering Design and Innovation Centre, College of Design and Engineering, National University of Singapore, Singapore, Singapore.

⁸Department of Electronic and Computer Engineering, The Hong Kong University of Science and Technology, Hong Kong, China. ⁹National Engineering Research Center of Electric Vehicles, Beijing Institute of Technology, Beijing, China. ¹⁰Department of Mechanical Engineering, Hong Kong Polytechnic University, Hong Kong, China. ¹¹Shanghai Frontiers Science Research Base of Intelligent Optoelectronics and Perception, Institute of Optoelectronics, Fudan University, Shanghai, China. ¹²State Key Laboratory of New Ceramics and Fine Processing, School of Materials Science and Engineering, Tsinghua University, Beijing, China. ¹³Ningbo Institute of Dalian University of Technology, Ningbo, China. ¹⁴Shenzhen Research Institute, City University of Hong Kong, Shenzhen, China. ¹⁵These authors contributed equally: Ya Huang, Jingkun Zhou, Pingchuan Ke, Xu Guo. ✉e-mail: zxie@dlut.edu.cn; keninzhu@cityu.edu.hk; xinge.yu@cityu.edu.hk

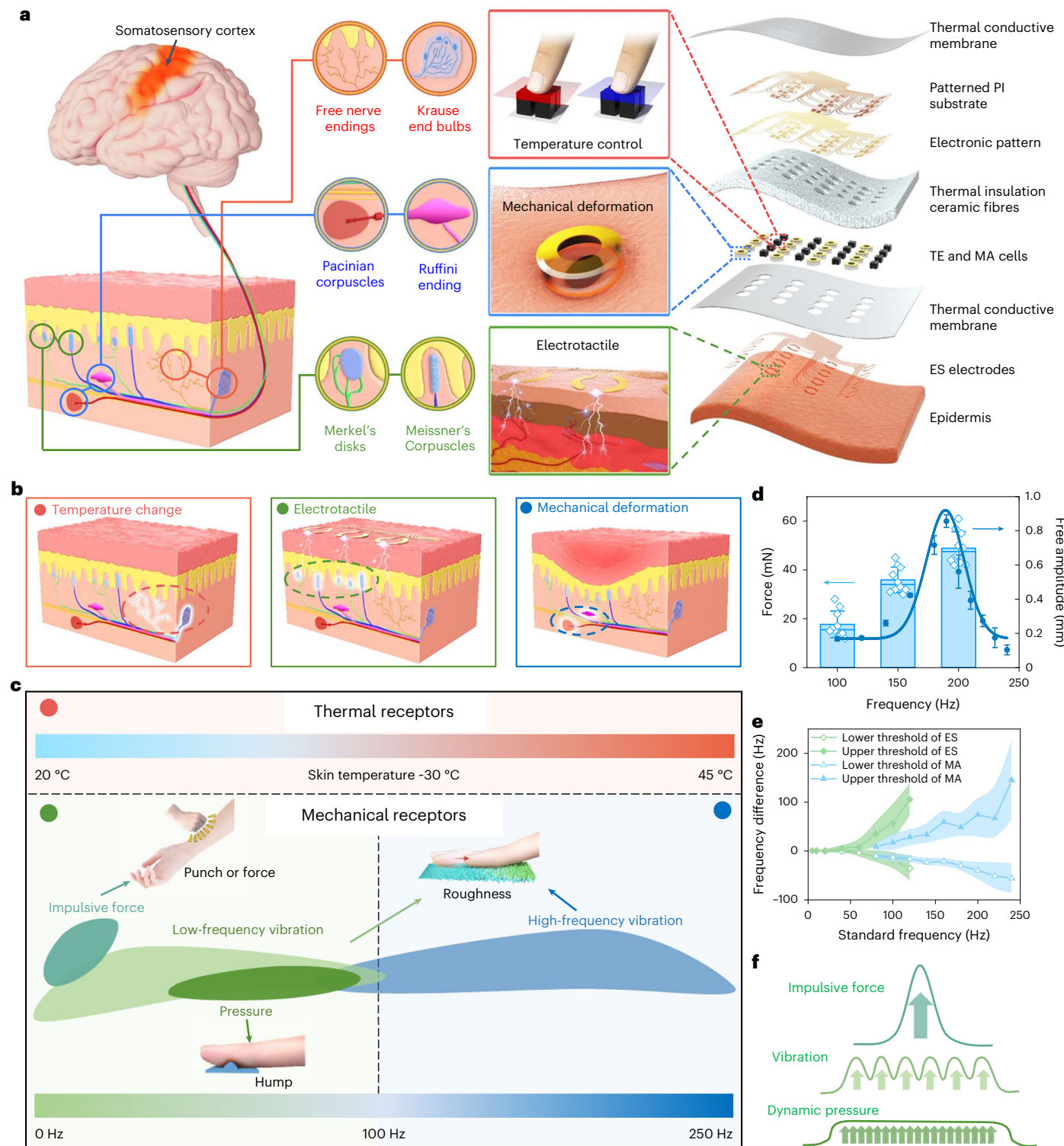


Fig. 1 | Multimode haptic feedback mechanism. **a**, Schematic of the neural tactile sensing system and the corresponding three stimulation modes. An exploded-view illustration of a device with 16 independently controlled multimodal haptic feedback units, each unit has a mechanical actuator (MA), two pairs of thermoelectric (TE) pellets and one pair of electrotactile (ES) electrodes. PI, polyimide. **b**, Selective stimulation on different receptors by three different feedback modes. **c**, Illustration of different tactile sensations

and related parameters for feedback. **d**, The force applied by the mechanical actuators and the free vibration amplitude activated at different frequencies. Centre line, median; bar height, mean; error bars, standard deviation (s.d.); $n = 10$ independent tests. **e**, Frequency discrimination results of electrotactile and mechanical vibration from the user study. Points, mean values; shading, s.d.; $n = 6$ independent tests. **f**, The description of impulse, vibration and dynamic pressure reproduced by electrotactile stimulation.

fine roughness, macro roughness, hardness, slipperiness and temperature¹³. Therefore, realistic haptic reproduction requires a feedback interface that includes as many of these dimensions as possible^{14–16}.

Temperature sensation depends on the heat flux that occurs when touching different objects, which can be related to the temperature and thermal properties of different surfaces¹⁷. Active cooling and heating

effects place high demands on the heat conductivity and heat dissipation capability of wearable devices¹⁸. Mechanical tactile feeling, which senses surface textures and forces, is decoded from spatiotemporally distributed pressure and vibration. For a haptic interface, the frequency should be tuneable within the sensitive range of human tactile sensations, which is 0–250 Hz (ref. 10). Research on frequency-leveraged actuators that can generate high output displacement even in small volumes has focused on resonance based on piezoelectric actuators¹⁹, linear resonant actuators²⁰ and eccentric rotating mass motors²¹. However, the amplitude of the displacement created by these actuators is coupled with the frequency, and greatly decreases outside of their resonant frequency⁷.

Pressure sensation usually requires large forces due to the strong damping effect of the skin, which is challenging to create with miniaturized actuators used for vibration²². Pneumatic and hydraulic systems are suitable for producing static pressure, but are not high-frequency vibration due to their low response speed²³. Since nerve activity codes all sensations, it should in theory be possible to create versatile tactile modalities by mimicking nerve signals^{24,25}. Electrotactile displays have been proposed as an alternative to conventional mechanical tactile displays without considering mechanical resonance^{26,27}. However, electrotactile modes are not precise enough to stimulate receptors located deep in the skin, such as Pacinian corpuscles that sense high-frequency vibration²⁸. In addition, electrotactile stimulation triggers a ‘harder’ or ‘sharper’ sensation, since all the receptors that receive a sufficient current fire together²⁹.

In this article, we report a skin-integrated multimodal haptic feedback interface that can stimulate different sensory receptors in the skin on the basis of the three actuation modes of temperature, mechanical deformation and electrotactile (Fig. 1a). Thermoelectric stimulation is used to control temperature changes on the skin, which reproduces the thermal feelings between the skin and objects. The sandwich structure of the devices achieves high heat dissipation to ensure good thermal feedback for activating free nerve endings or Krause end bulbs. Mechanical sensations are achieved by creating skin deformations using mechanical actuators, targeting the deep touch sensed by Pacinian corpuscles and Ruffini endings⁷, and electrotactile stimulation is used to create nervous activity of the shallower Merkel’s discs and Meissner’s corpuscles (Fig. 1b)^{14,30,31}. The interaction between electrotactile and mechanical vibrators can enhance their integrated performance compared to a single mode, improving the fidelity of virtual mechanical tactile sensations over a frequency range of 0–250 Hz. We test the capability of the developed multimodal haptic feedback interface when located on a person’s wrist, arm and palm by comprehensive user studies, and can create virtual tactile sensations of fine roughness, macro roughness, slipperiness and temperature.

Mechanism of multimodal tactile sensation stimulation

The haptic feedback unit operates with three feedback modes: thermal feedback based on two pairs of thermoelectric pellets, mechanical feedback based on a miniaturized mechanical actuator and electrotactile feedback based on thin and soft Au electrodes (Supplementary Fig. 2). The difference in thermal conductivity coefficient between skin and the targeted object results in the perceptions of warm or cold feeling for different materials. Extended Data Fig. 1 shows the temperature changes simulated when fingers touch different materials in which the temperature change is greatly influenced by the thermal conductivity coefficient of the targeting materials. For example, touching 2-mm-thick brass (thermal conductivity coefficient, $k = 116 \text{ W m}^{-1}\text{K}^{-1}$) causes a temperature change over 7 °C in 5 s of touching and over 8 °C after 30 s of touching, while the temperature change is less than 3 °C for touching polydimethylsiloxane (2 mm thick, $k = 0.15 \text{ W m}^{-1}\text{K}^{-1}$) and less than 2 °C for touching cotton ($k = 0.03 \text{ W m}^{-1}\text{K}^{-1}$) after 30 s (Supplementary Fig. 3). Additionally, the temperature change can vary

according to changes in the geometric size of materials or skin (Supplementary Figs. 4 and 5). In our device, the thermoelectric pellets modify the interface temperature between the top layer of the device and skin according to the virtually touched materials in the range of 20–45 °C (Fig. 1c). The device produces active cooling and heating sensations based on the Seebeck effect¹⁷.

Vibratory cues, in conjunction with spatial cues, can be used to perceive different tactile feelings of the surface of touched objects. To achieve mechanical tactile representation, we selected electro-mechanical actuators on the basis of Lorentz force to create physical skin deformation and provide a sensation of high-frequency vibration (Fig. 1a). In this design, a polyimide sheet with a cantilever structure holds a magnet for vibration to stimulate the mechanoreceptors under the skin (Fig. 1b and Supplementary Fig. 6)^{32,33}. However, the vibration travel amplitude of mechanical actuators is strongly affected by the working frequency. In Fig. 1d, the maximum travel amplitude of the actuator is above 0.8 mm at the resonant frequency around 200 Hz, but the travel amplitude reduces to around 0.2 mm at 100 Hz when activated by the same voltage. The maximum force applied by the vibration is up to 50 mN at around 200 Hz, but the force reduced to around 20 mN at 100 Hz (ref. 34).

Electrical pulse depolarizes nerve fibres to create tactile sensations. The period of the nerve’s activity synchronizes with the period of vibration sensation (Supplementary Fig. 7)³⁵. To study the frequency discrimination ability of electrotactile and mechanical vibration, we conducted a user study in which participants were asked to compare a standard frequency with other frequencies lower or higher than the standard. We increased or decreased the frequency from standard frequency for comparison until participants could distinguish them, and the threshold frequency difference at different standard frequency is shown in Fig. 1e. We observed that the difference in electrotactile frequency is small at low frequency (within 20%), especially below 80 Hz. However, the discrimination threshold of electrotactile frequency began to increase beyond 80 Hz, and participants were even able to discriminate 120 and 200 Hz in the electrotactile mode. On the other hand, the lower and upper discrimination thresholds of mechanical vibration below the standard frequency of 140 Hz are still within 20 and 30%, respectively.

Meissner’s and Pacinian corpuscles are two types of mechanical receptor that respond to mechanical vibrations. Meissner’s corpuscles are located in the shallow dermis near epidermis, while Pacinian corpuscles are in the hypodermis or deep part of the dermis^{10,11}. They can be activated at their typical sensitive frequency, where Meissner’s corpuscles are stimulated by the vibration below 100 Hz (most sensitive between 20–40 Hz) and Pacinian corpuscles are activated higher than 80 Hz (most sensitive between 200 and 250 Hz)²⁹. However, electrotactile stimulation is considerably more effective in stimulating the superficial nerves, as evidenced by the electrical current and field distributions simulated beneath the skin (Extended Data Fig. 2 and Supplementary Fig. 8). As a result, Meissner’s corpuscles are inevitably coactivated in high-frequency electrotactile mode due to the stronger electrical pulse depolarization in the shallow region of the dermis. The brain misinterprets the activation of Meissner’s corpuscles with Pacinian corpuscles at high-frequency electrotactile mode, leading to difficulties in frequency discrimination. To overcome this limitation, we propose a hybrid method of applying mechanical and electrotactile modes simultaneously, in which mechanical actuators selectively stimulate Pacinian corpuscles while the electrotactile mode targets Meissner’s corpuscles (Fig. 1c).

Users can feel a force applied to the skin in each electrotactile pulse and it is easy for them to discriminate each pulse in the frequency range lower than 10 Hz. An electric pulse with high intensity can activate a vigorous impulsive force on the skin, which can be used to mimic some punching behaviours in virtual situations (Fig. 1f). With the increase of frequency, applied force with short intervals is easy to feel like vibration

on the skin. Furthermore, when users feel a continuous force (either in constant or varied format) applied on their skin, dynamic pressure is created. Typically, the continuous pressure sensation, when skin receives continuous force and cannot discriminate each pulse, is activated by electrotactile mode (Fig. 1f)³⁶. The dynamic pressure activated by electrotactile mode is properly composed of slight sensations of vibration, such as skin sliding over a hump (Fig. 1c)³⁷.

In our multimode haptic feedback interface, electrotactile mode mainly stimulates Merkel's discs and Meissner's corpuscles to create the tactile feelings of pressure, vibration and impulsive force (Fig. 1c)^{14,34}. A strong electric pulse can activate an impulsive force on the skin, which can be used to reproduce some dynamic interactions between skin and objects. The impulsive force created by electrotactile mode is much higher than that provided by mechanical actuators. Electrotactile and mechanical deformation can work together to provide a wide frequency range of vibration related to tactile sensation on different surfaces. When integrated with thermoelectric actuators, the whole device can effectively provide multiple tactile sensations, including punching, vibration, feeling pressure or a hump, warmth and cold.

Design of multimodal haptic interface

The integration of thermal feedback, mechanical vibration and electrotactile feedback in skin-integrated interfaces can provide diverse tactile sensations to users in virtual reality (VR) and/or augmented reality while preserving their ability to interact with the real world (Fig. 2a). The right part of Fig. 1a shows the schematic illustration of the versatile haptic interface, where the three types of actuator in array formats, electrical interconnects, thermal insulation fibres and the soft thermal conductive (TC) substrate are integrated. In the haptic interface, a thin layer of laser-cut Cu–PI (18 and 12.5 μm), supported by a soft silicone TC substrate (mixed with carbon compounds and metal-oxide compounds, 300–1,000 μm thick, Supplementary Fig. 9), serves as electrical interconnects to create a compact route for closely spaced mechanical actuators and thermoelectric pellets (Supplementary Fig. 2). After mechanical actuators and thermoelectric pellets are welded, thermal insulation ceramic microfibres fill in the gaps among the mechanical actuators and thermoelectric pellets to inhibit the heat flow back (Supplementary Fig. 10). Another layer of TC thin film with an opening on each mechanical actuator encapsulates the device and serves as the supporting layer for electrotactile electrodes. The mechanical property of the encapsulation layer has no obvious effect on the resonance frequency of the mechanical actuators (Supplementary Fig. 11). Photo-defined Cr–Au–PI thin film (5 nm, 200 nm and 2 μm) patterns act as soft electrotactile circuits. Another layer of polyimide (2 μm thick) with selective dry etching allows for encapsulating the interconnects and leaves the electrode open to contact with the skin. The multimodal haptic feedback interface can be designed and customized into various shapes with different actuator arrays. Figure 2b–d shows three types of device: a strip with a 2 × 4 feedback units array, a patch with a 4 × 4 feedback units array and a palm format with distributed actuators over the hand, respectively. The detailed dimension and weight of different devices are summarized in Supplementary Table 2. These devices can be directly interfaced with various body locations such as the wrist, arm, palm and other positions (Supplementary Fig. 12). The electric circuits on different layers remain stable even after being bent for 500 cycles (Supplementary Fig. 13).

The multimodal haptic feedback patch can be powered by coin-sized batteries (Supplementary Fig. 14) and wirelessly operated by thin and miniaturized wristband-type flexible circuits (Fig. 2e). Extended Data Fig. 3 shows the block diagram of the control circuit for the multimodal haptic feedback interface. The microcontroller unit (MCU) communicates with personal computers through a bluetooth low energy (BLE) module to receive the commands from the personal computer and generate corresponding electrical signals to drive the three feedback modules. The voltage conversion module consists of a

low dropout regulator (LDO), a boost converter and a buck converter. The LDO steps down the input voltage to 3.3 V to power the MCU, while the boost converter module steps up the input voltage into high output voltage to drive the electrotactile module. The buck converter is used to convert the input voltage to a low level of 2.5 V to enhance the current output capability, which can drive the actuator and thermoelectric modules. The operation of the thermal feedback is associated with controlling the input power for the thermoelectric pellets with either positive or negative voltage to realize heating or cooling.

It is challenging for skin-integrated devices to have a good cooling effect due to their limited heat dissipation capability, resulting in an obvious temperature increase in cooling process caused by residual heat. To improve the thermal dissipation performance, a sandwich structure is designed (Supplementary Fig. 15). Two sides of the device are encapsulated by soft TC materials with a relatively high thermal conductivity coefficient ($k \geq 1.93 \text{ W m}^{-1}\text{K}^{-1}$). The inner part between the two TC layers is filled with a thermal insulation material (ceramic microfibres, $k \leq 0.035 \text{ W m}^{-1}\text{K}^{-1}$) to reduce heat conduction between the two TC layers. The sandwich design can maintain a large temperature difference between the two TC layers, which is confirmed by simulation results and detected infrared photographs (Supplementary Fig. 16). Figure 2f shows time-dependent temperature profiles of both cooling and heating modes on a 4 × 4 patch under various power inputs. Both simulation and experiment results indicate that the device can produce desirable temperature changes for cooling and heating rapidly (Extended Data Fig. 4 and Supplementary Fig. 17). To investigate the active cooling and heating effects, the temperature change progress is simulated for the device mounted on skin (Extended Data Fig. 5), where the heat dissipation progress occurs on the TC layer contacting with air (outer TC layer). Figure 2g shows the influence of the thickness and heat dissipation structure (Supplementary Fig. 18) of the outer TC layer in the cooling progress on the interface between the device and skin. Increasing the thickness of the outer TC layer and adding the heat dissipation structure can improve the cooling effect and inhibit the temperature increase caused by residual heat. Moreover, higher air convective heat transfer can enhance the cooling effect due to better heat dissipation (Supplementary Fig. 19). On the other hand, increasing the thickness of the outer TC layer enhances the heating capability of the interface adhered to the skin (Supplementary Fig. 20). For a 1-mm-thick outer layer, the temperature decreases over 7 °C, showing a negligible increase within the following 10 s in the cooling progress (Extended Data Fig. 5). An embedded design of the outer TC layer can effectively reduce the thickness of the device without reducing the heat dissipation effect (Supplementary Fig. 21). Finally, the device can achieve a maximum ΔT of more than 7 °C for the cooling mode and 12 °C for the heating mode with an input current of around 1 A within 5 s (Fig. 2h).

Tactile sensation reproduced by three feedback modes

A group of volunteers participated in a test in which they reported their feelings of touching different materials by feeling the different thermal properties and comparing them with real materials (Fig. 2i). In the cooling mode with a power density of around 100–130 mW, the participants could easily feel chilly ($\Delta T > 4.5^\circ\text{C}$), which convinced them of touching materials with a thermal conductivity coefficient greater than $1 \text{ W m}^{-1}\text{K}^{-1}$, such as quartz glass ($k = 1.4 \text{ W m}^{-1}\text{K}^{-1}$), stainless steel ($k = 25 \text{ W m}^{-1}\text{K}^{-1}$) and brass ($k = 116 \text{ W m}^{-1}\text{K}^{-1}$). Reproducing the tactile sensation of thermal insulation materials is more complicated than that of TC materials. Computational results reveal that materials with thermal conductivity coefficient less than $0.1 \text{ W m}^{-1}\text{K}^{-1}$ may also result in a slight temperature decrease (Extended Data Fig. 1). Considering the microstructures and textures of the materials, the physical touch feeling of these materials such as cardboard ($k = 0.07 \text{ W m}^{-1}\text{K}^{-1}$), cotton cloth ($k = 0.06 \text{ W m}^{-1}\text{K}^{-1}$) and plastic foam ($k = 0.03 \text{ W m}^{-1}\text{K}^{-1}$) is often warm³⁸. Due to the high thermal conductivity coefficient of our

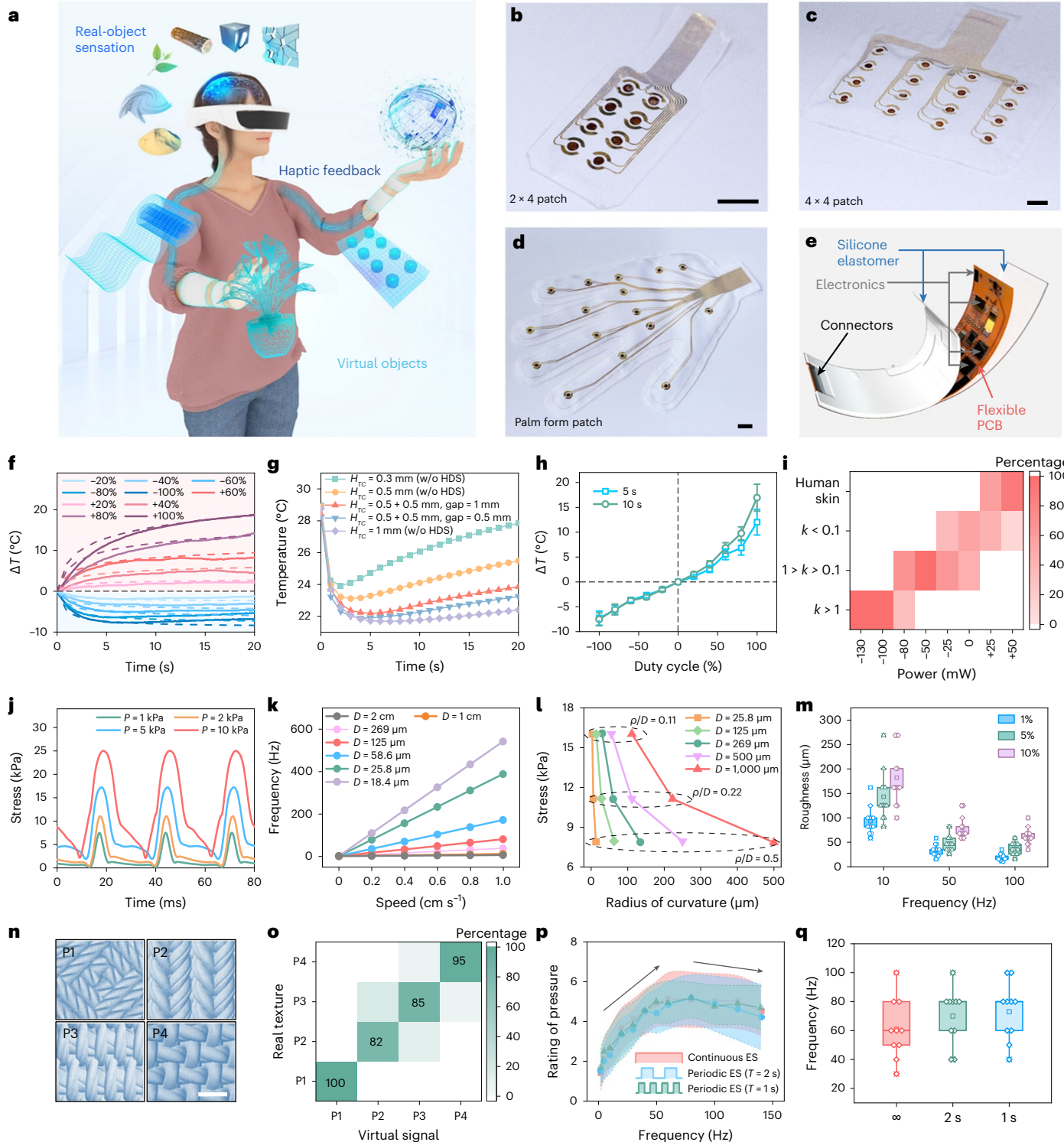


Fig. 2 | Operation of the multimodal haptic patch. **a**, Schematic illustration of a user feeling real-object sensations from the haptic feedback interface in VR. **b–d**, Photographs of different haptic feedback units arrays, including a 2×4 patch (**b**), 4×4 patch (**c**) and palm-form patch (**d**). Scale bars, 1 cm. **e**, 3D illustration of the wireless control circuits. PCB, printed circuit board. **f**, Time-dependent temperature changes under different power density. Solid lines, experimental data; dotted lines, simulation data. **g**, Thermal simulation of cooling effect when devices were attached on the skin with different outer heat dissipation surfaces. w/o, without. **h**, The value of the temperature difference 5 and 10 s after activation. Data are presented as mean values \pm s.d.; $n = 5$ independent tests. **i**, User study results of judging the temperature change on the surface with real materials ($k = 0-0.1$, roughly $0.1-1$ and $>1\text{W m}^{-1}\text{K}^{-1}$). Different temperature changes can be controlled by the power applied on each unit, where 'negative power' represents the cooling mode. **j**, The time-dependent stress curve felt by the 1cm s^{-1} moving finger on the surface with a roughness of $269\text{ }\mu\text{m}$. **k**, The frequency change versus finger moving speed on surface with different roughness. **l**, The stress collected from dynamic simulation when the skin slides over different morphologies. **m**, Summary of the roughness sensation of sandpapers in the user study with different virtual rough surfaces created in electrotactile mode. Square, mean; centre line, median; box limits, upper and lower quartiles; whiskers, $1.5 \times$ interquartile range; points, outliers; $n = 13$ independent spots. **n**, Photographs of four textures used in user studies for distinguishing the patterns created on actuator arrays. Scale bar, 5 mm. **o**, The accuracy in discriminating the four textures. **p**, The rating levels of pressure sensation created by electrotactile mode at different frequency. Pointes, mean values; shadings, s.d.; $n = 10$ independent tests. **q**, The box plot of the electrotactile frequency that activates dynamic pressure in the user study. Square, mean; centre line, median; box limits, upper and lower quartiles; whiskers, $1.5 \times$ interquartile range; points, outliers; $n = 10$ independent spots.

finger on the surface with a roughness of $269\text{ }\mu\text{m}$. **k**, The frequency change versus finger moving speed on surface with different roughness. **l**, The stress collected from dynamic simulation when the skin slides over different morphologies. **m**, Summary of the roughness sensation of sandpapers in the user study with different virtual rough surfaces created in electrotactile mode. Square, mean; centre line, median; box limits, upper and lower quartiles; whiskers, $1.5 \times$ interquartile range; points, outliers; $n = 13$ independent spots. **n**, Photographs of four textures used in user studies for distinguishing the patterns created on actuator arrays. Scale bar, 5 mm. **o**, The accuracy in discriminating the four textures. **p**, The rating levels of pressure sensation created by electrotactile mode at different frequency. Pointes, mean values; shadings, s.d.; $n = 10$ independent tests. **q**, The box plot of the electrotactile frequency that activates dynamic pressure in the user study. Square, mean; centre line, median; box limits, upper and lower quartiles; whiskers, $1.5 \times$ interquartile range; points, outliers; $n = 10$ independent spots.

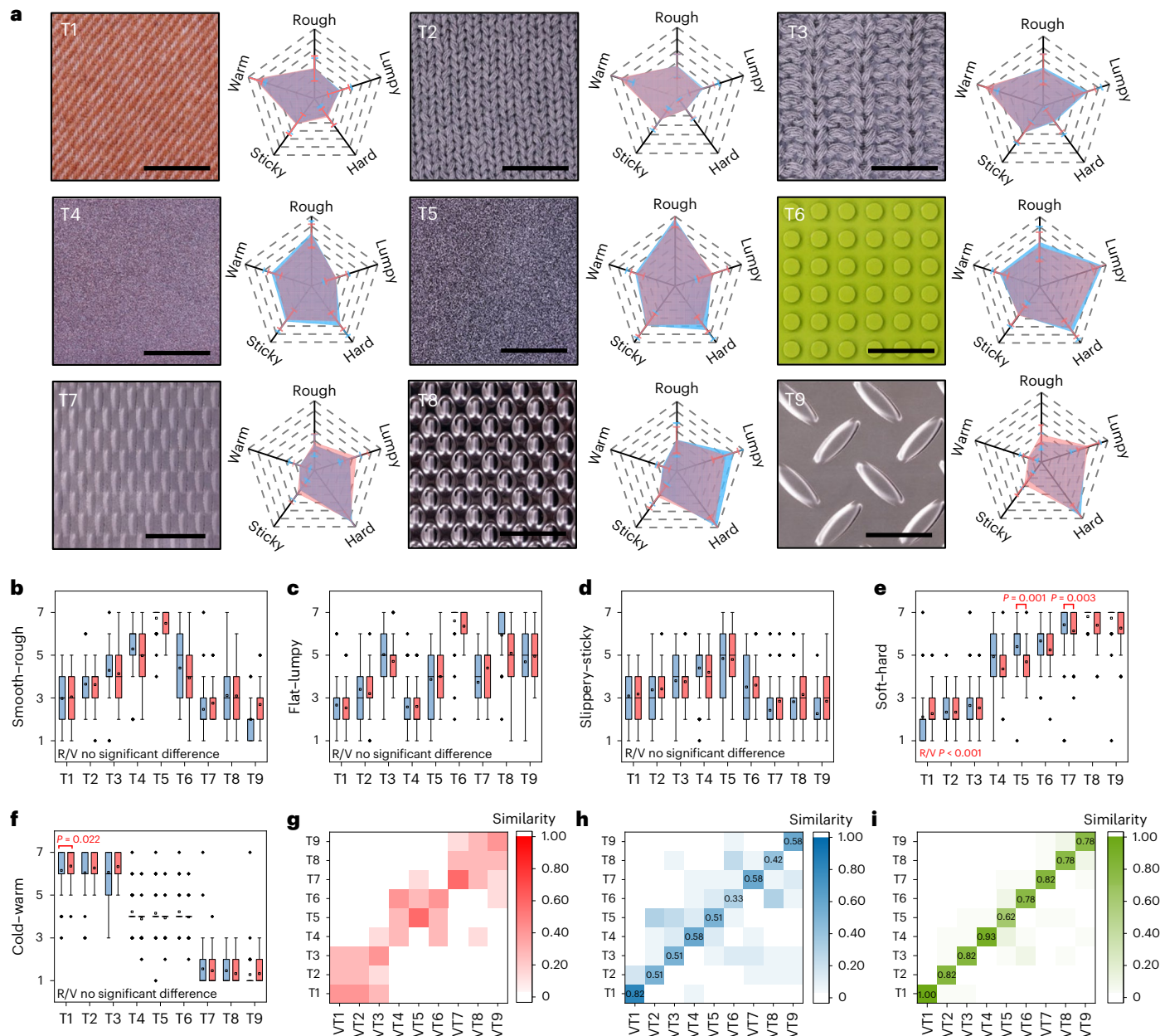


Fig. 3 | User study of multidimensional scaling textures. **a**, Nine different materials tested in user study, including fabric, sandpapers, stainless steel and plastics with different roughnesses and patterns. The right radar diagrams are the average rating values of real and virtual textures in five dimensions: soft-rough, flat-lumpy, soft-hard, slippery-sticky and cold-warm obtained from minimum data set user studies. The box plots of five-dimensional ratings of these nine textures. Blue shadings, true textures red shadings, virtual textures. Scale bar, 2 cm. **b**, Smooth-rough. **c**, Flat-lumpy. **d**, Soft-hard. **e**, Slippery-sticky. **f**, Cold-warm.

The scores for real and virtual textures are listed in pairs. Square, mean; centre line, median; box limits, upper and lower quartiles; whiskers, $1.5 \times$ interquartile range; points, outliers; $n = 45$ independent tests. Two-way repeated-measures analysis of variance was performed on data for each modality. **g-i**, The results of the user study when distinguishing different materials with only thermal feedback (**g**), only mechanical feedback (electrotactile and mechanical deformation) (**h**) and both thermal feedback and mechanical feedback (electrotactile and mechanical deformation) (**i**).

encapsulation layers, the devices should heat up slightly to mimic the heat flux change when skin touch materials with low thermal conductivity coefficients (Supplementary Fig. 22). Therefore, the warming mode relies on the combination of theoretical data and extensive user studies (Fig. 2*j*).

We simulated the behaviour of a finger sliding across surface with varying levels of fine roughness (Fig. 2*j* and Extended Data Fig. 6), where the roughness perceptions resulting from vibratory stimuli are sensitive to dynamic stimulation caused by finger movement. The change in stress frequency on the finger is strongly affected by the sliding speeds and the surface roughness (Fig. 2*k*). Surface with

lower roughness represents smaller spacing among particles, which can lead to higher frequency responses during sliding owing to the smaller intervals as the sliding speed increases. On the same roughness surface, a sharper morphology can cause a larger stress (Fig. 2*l*). We tune the frequency and amplitude of the electrotactile mode to activate different low-frequency vibrations to reproduce the sensation of fine roughness. Figure 2*m* presents the results in which participants compared the stimulated roughness on the electrode with the real tactile sensation of touching sandpapers. The results reveal that a higher frequency and lower amplitude in electrotactile mode can reproduce the tactile sensation of touching less rough sandpapers.

When the electrotactile intensity is low, the sensation is similar to that of mechanical stimulation. Sometimes, participants could not tell which was electrotactile and which was mechanical stimulation. However, when the intensity becomes high, they can distinguish the sensation of electricity clearly. Mechanical stimulation offers a softer feeling, while electrotactile stimulation offers a stronger or sharper feeling. This may be because the electricity stimulates localized nerves synchronously, while mechanical deformation leads the force to be distributed to a large area, stimulating surrounding mechanoreceptors with different intensities³⁹. Thus, mechanical vibration is more suitable for stimulating the tactile sensation when a finger moves across a soft surface, and electrotactile mode can be added to increase the ‘harder’ roughness in some virtual textures. In addition, vibration activated by electrotactile mode and actuators can be programmably controlled on the basis of different texture patterns. Figure 2n shows four texture patterns of soft materials reproduced by the mechanical actuators array (Supplementary Fig. 23), which is easy for participants to distinguish the shape (Fig. 2o).

Tactile feeling obtained from the macro-morphology of different surface, such as humps, are closely related to pressure sensations. As we discussed earlier, undistinguished pulse can produce continuous pressure sensation on the skin to mimic humps. We conducted a user study to rate the pressure sensation activated by three kinds of electrotactile mode, including continuous and periodic electrotactile modes with periodic cycles of 2 and 1 s (Fig. 2p). The average rating levels of pressure sensation in these three modes at different frequency follow a similar pattern. The rating levels increased sharply with the increase of frequency lower than 80 Hz but slightly reduced due to the increase of tickle or tingling feeling caused by an electrotactile frequency of more than 100 Hz. We collected the frequency at which participants rated the highest level of pressure, mostly ranging from 40 to 100 Hz as shown in Fig. 2q. We point out that the surface morphology can be divided into fine roughness and macro roughness. In the dynamic touching behaviours where the skin and object are in relative motion, fine roughness can be represented by the tuneable vibration produced by mechanical actuators and electrotactile stimulators, and macro roughness can be represented by the electrotactile period of activation (Supplementary Fig. 24). Therefore, changing the portfolio of the activated actuators allows to realize both macro roughness and fine texture sensations with a static contact between the device and skin.

To further compare the resolution and density of our skin-integrated haptic feedback interface with other published works based on different haptic feedback mechanisms, we summarized the geometric size, density and functions of different systems in Supplementary Table 4.

Texture recognition with multimodal haptic interface

When we touch real objects, our skin gathers diverse information about the interactions, which is crucial for decoding the tactile sensations.

Fig. 4 | Demonstration of the multimodal haptic feedback VR system.

a, A schematic picture of a user wearing a VR headset for visual and auditory feedback. The Leap Motion tracks the movement of her hand and send messages to the computer where the control centre can transmit commands to the haptic feedback patches for stimulating haptic feedback on the hands and arms when touching different virtual objects. **b**, The user simulates using an alcohol wet wipe on the hand, where the temperature decreases to simulate the evaporation of alcohol and the palm feels slight force produced by mechanical actuators. Heat maps present the distribution of the temperature change and mechanical vibration amplitude in the palm-form device, where P1 to P16 are the positions of 16 multimode haptic units. **c**, The user touches the surface of a virtual book where the temperature decreases due to the lower book temperature and user’s fingers feel the roughness activated by electrotactile mode. Heat maps present the distribution of the temperature change and the electrotactile intensity

The richness of these interaction cues is often missing from many single-mode haptic feedback interfaces, resulting in a less satisfying and immersive experience. Feeling multidimensional tactile sensation from haptic feedback interfaces can create the perceptual illusion that one is touching a real surface. To evaluate the virtual tactile perception production ability of our multimode haptic interface devices, we conducted a series of user studies. Figure 3a shows nine typical materials including fabric, sandpapers, plastics and stainless steel used in our user study, which have diverse fine textures, morphology and patterns. Wool fabric is a soft material often used for clothing, which is always felt as warm when touched. By contrast, steel is a rigid metal that causes an obvious temperature decrease when touched.

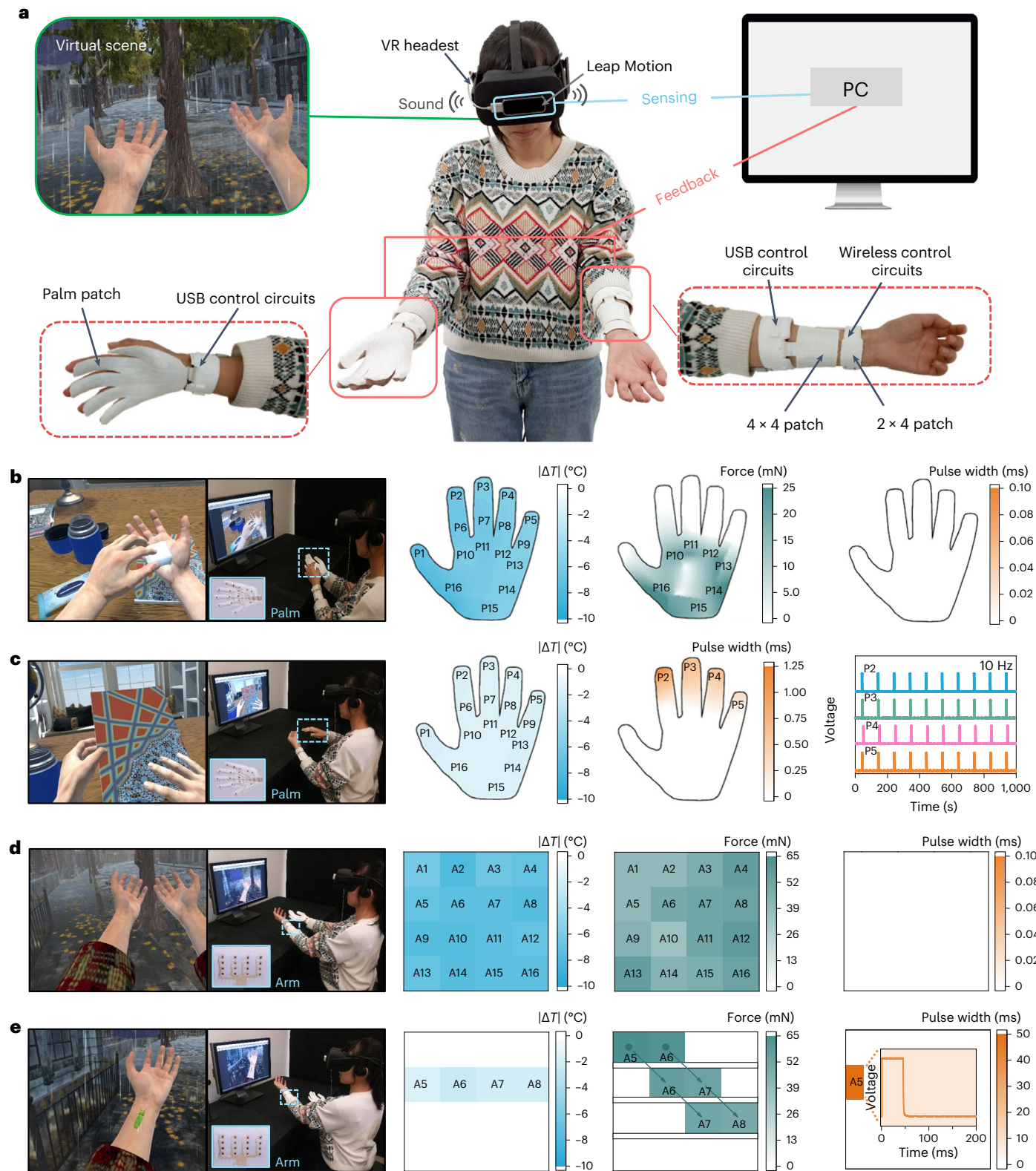
Virtual textures rendered with the data-driven method are more realistic than those generated with periodic signals⁵. To prove the reappearance ability of our haptic feedback interface and convert the texture signal of different surfaces into digital signals that can be processed and transmitted by a computer, we recorded pressure signals and acceleration signals from real touching behaviours to create texture models (Supplementary Fig. 25)⁵. In practical situations, feelings of fine texture information can be achieved by moving fingers over the surface of an object to get a vibration sensation. In our haptic interface, the feedback of fine textures can be reproduced by adjusting the pulse width and the frequency of electrotactile and mechanical vibration to simulate the intensity of the force and discriminate the vibration. The acceleration signal is used to analyse the small vibrations generated by the micro-morphology of the materials during finger sliding, which is related to the fine roughness and slipperiness of the surface (Supplementary Fig. 26). The mechanical actuator exhibits high resolution at high frequencies and can be used to reproduce the high-frequency vibration signals collected by accelerometers. Real vibration signals can be encoded by pulse width modulation signals to drive mechanical actuators to mimic the real vibration (Supplementary Fig. 27). Low-frequency vibration signals can be reproduced by tuneable electrotactile mode. As the finger passes over different surfaces, the macro-morphology of textures can be reflected in the periodic change of pressure, such as T3, T6, T7, T8 and T9 (Supplementary Fig. 28). To produce a sensation similar to the pressure change on the skin, we determine the electrotactile period cycle on the basis of the full-width at half-maximum of the pressure peak. The intensity of each cycle of electrotactile mode is controlled by the pressure value. Then, the macro-morphology related to pressure sensation is generated by periodic electrotactile mode for mimicking the behaviour of skin sliding across these humps (Supplementary Fig. 29).

We conducted a within-subject study to evaluate the performance of tactile simulation using our device. We designed a user-perception experiment with two separated parts, one for subjective rating and another for tactile matching⁴⁰. In the first subjective rating experiments, participants placed their palms firmly on the multimodal haptic feedback interface to perceive the virtual texture during the study. The haptic feedback stimuli of nine textures were individually provided to

in the palm-form device. Because the four fingers moved simultaneously, the frequency of stimulation is the same on the four fingertips (P2 to P5), corresponding with the same electrical waveforms. **d**, The user feels the shaking of cloth under a strong wind and chill due to heat transfer with a haptic feedback patch attached on the arm, where A1 to A16 are the positions of 16 multimode haptic units in the 4 × 4 patch. The sleeve flapped at the same time, which was produced by the mechanical actuators. Heat maps present the distribution of the temperature change and mechanical vibration amplitude in the device. **e**, The user feels a worm fall on their arm and crawl. The first impact felt by the arm at the point the worm fell on the arm (A5) was activated by the electrotactile mode, then the temperature decreased slightly due to heat transfer from the worm and the crawling behaviour was activated by the mechanical actuators (A5, A6 → A6, A7 → A7, A8).

the participants at one time in randomized order. The stimuli conditions (that is, real or virtual) were in a counter-balanced order. Fifteen participants completed the adjective ratings for 18 textures (nine real, nine virtual) in five dimensions—fine roughness (smooth–rough), macro roughness (flat–lumpy), slipperiness (slippery–sticky), hardness (soft–hard) and temperature (cold–warm) (on a scale from 1 to 7)—which were chosen on the basis of the psychophysical dimensions applicable to the perception of textures⁴¹. The participants rated all textures

along each scale before proceeding to the next scale. The average rating levels in these five dimensions of each texture were shown in the radar charts of Fig. 3a, where the levels for virtual texture showed a similar shape to that of real texture in most textures. The original adjective rating data in five dimensions are shown in the box plots of Fig. 3b–f, where real textures and virtual textures are listed in pairs. A two-factor repeated-measures analysis of variance was performed separately on the five sets of adjective ratings using texture and virtual and/or



real as factors⁴⁰. When comparing across textures, the differences in rating of smooth–rough ($F(8, 352) = 102.204, P < 0.001, \eta_p^2 = 0.699$), flat–lumpy ($F(8, 352) = 86.577, P < 0.001, \eta_p^2 = 0.663$), slippery–sticky ($F(8, 352) = 38.543, P < 0.001, \eta_p^2 = 0.467$), soft–hard ($F(8, 352) = 240.158, P < 0.001, \eta_p^2 = 0.845$) and cold–warm ($F(8, 352) = 428.854, P < 0.001, \eta_p^2 = 0.907$) were found to be statistically significant. When comparing virtual and real texture, the differences in smooth–rough ($F(1, 44) = 0.402, P = 0.529, \eta_p^2 = 0.009$), flat–lumpy ($F(1, 44) = 2.150, P = 0.150, \eta_p^2 = 0.047$), slippery–sticky ($F(1, 44) = 2.828, P = 0.100, \eta_p^2 = 0.060$) and cold–warm ($F(1, 44) = 0.194, P = 0.662, \eta_p^2 = 0.004$) were not found to be statistically significant, proving that our haptic feedback provides good virtual tactile sensations in these four dimensions. However, the difference in soft–hard was found to be statistically significant ($F(1, 44) = 25.487, P < 0.001, \eta_p^2 = 0.367$), and the rated hardness of the virtual textures did not correlate well with the real textures. Previous studies have reported that users found it difficult to discern the hardness of materials when they touched a flat surface but could clearly feel both unevenness and hardness of the same material when they perceived a change in shape or morphology on the surface.¹⁴ The changes in friction sensation are related to the sliding acceleration of fingers on the surface, and sometimes participants were unable to clearly distinguish the difference between friction and fine roughness when they moved their fingers on a surface¹⁴. Stimulation of high-frequency components corresponding to the acceleration of hand movements could produce a natural sliding feeling³⁹.

In the tactile matching section, virtual textures activated by three conditions, only thermal feedback, only mechanical feedback (mechanical deformation and electrotactile) or both thermal feedback and mechanical feedback (mechanical deformation and electrotactile), were given to participants in a randomized order. Then participants were asked to choose the most similar real materials on the basis of their haptic sensations obtained from the feedback device. Figure 3g shows the test results of distinguishing these materials only by temperature cues, where T1–3, T4–6 and T7–9 are three groups that could not be distinguished. Figure 3h shows the results of distinguishing these materials only by mechanical information produced by mechanical actuators and electrotactile stimulation. Compared to the single mechanical haptic feedback, the multimodal haptic interface allows users to achieve higher accuracy in recognizing different materials (Fig. 3i). The improvement of 18, 31, 31, 35, 11, 45, 24, 36 and 20% for T1 to T9 textures, respectively, demonstrate the advantages of producing rich tactile information in multimodal haptic feedback interfaces.

Integration of haptic interface with VR applications

Figure 4a demonstrates the use of the multimodal haptic interface for experiencing interactions with the virtual world in immersive VR applications (Supplementary Video 1). The user wears a VR headset and three soft haptic feedback patches on her wrist, arm and hand. The commercially available VR head-mounted device (HMD) provides visual and/or auditory information and hand motion captures. The haptic feedback patches, synchronized with the HMD, generate tactile sensations from the video contents. The video and auditory contents are created by Unity3D game engine. Due to the skin-integrated design of our haptic feedback interface, it is easy for the engine synchronized with the motion controller of the HMD to trace the user's hand movements, detect collisions between the virtual hand and the virtual object, and send commands to the haptic interfaces for corresponding tactile feedback. We demonstrate applications in both indoor and outdoor scenes. For the indoor scenes, several materials, including a wet tissue with 75% alcohol, a notebook with smooth and rough surface areas, a wooden tabletop and a cup with hot water, are presented for the user to interact with (shown in Fig. 4b,c and Extended Data Fig. 7). For the outdoor scenes, several different types of weather, including breeze, strong wind, heavy rain and light rain, as well as the sensation of a falling

insect, are demonstrated (Fig. 4d,e and Extended Data Fig. 8). In addition to tactile sensation on texture, impulsive force is an effect haptic feedback in virtual reality (VR) for mimicking collisions with virtual objects. In outdoor scenes, impulse feedback is effective in reproducing the tactile sensation when raindrops fall on the skin. During the immersive experience, users can feel dynamic changes of temperature, force, texture and vibration, which provide rich tactile sensations of the virtual world.

We further conducted a user study with four scenes for participants that associate disinfection with 75% alcohol tissue, pouring hot water into a glass bottle, strong wind and heavy rain, to rate the similarity of their haptic feedback perception with real tactile feelings and compare the difference between visual-auditory feedback and real sensation. (Extended Data Fig. 9) The integration of visual-auditory and haptic feedback achieved higher similarity levels than single-mode feedback. These rich interactions and multisensory feedback make it possible to bring the virtual world closer to reality, allowing users to interact with things in their daily life and get a more immersive experience.

Conclusions

We have reported a thin and soft multimodal haptic feedback interface that can be directly integrated with the skin. The device incorporates thermal, mechanical and electrical feedback modes that target different receptors in the skin to achieve versatile haptic sensations for force, temperature and texture rendering. Evaluation in user studies of the tactile sensations created by our interface show high fidelity in the dimensions of fine roughness, macro roughness, slipperiness and temperature compared to tactile sensations produced from real objects. Hardness sensation could be further improved by increasing the density and spatial distribution of pressure feedback. The development of a skin-integrated multimodal haptic feedback interface could allow users to interact with the virtual world in a more immersive way, with potential applications in online working, entertainment, surgical robots and industrial training.

Methods

Fabrication of the mechanical actuators

The diameter of the mechanical actuator was 5 mm. The ring of the actuator was fabricated by three-dimensional (3D) printing with ultraviolet-curable resin (inner diameter of 4 mm, outer diameter of 5 mm, thickness of 1 mm). A polyimide supporting layer (40 µm thick) was designed and laser cut into a semicircular disc. A permanent magnet with a diameter of 2 mm and a thickness of 0.5 mm was glued on the cantilever-like platform of the semicircular polyimide disc and then attached to the resin ring with glue. A coil (inner diameter of 2 mm, outer diameter of 5 mm, thickness of 0.25 mm) with 50 turns of Cu wires with a diameter of 50 µm was glued on the other side of the ultraviolet-curable ring, and the cavity between the ring and the magnet allowed the magnet to vibrate freely. After assembling all parts, the overall dimension of the actuator was 5 mm in diameter and 1.5 mm in thickness.

Fabrication of the electrotactile electrodes

The fabrication process for the flexible electrodes started on a glass substrate, which was used without any further treatments. First, poly(methyl methacrylate) solution was spin-coated on the glass as a sacrificial layer (annealed at 200 °C for 20 min), then a thin layer of polyimide (2 µm, annealed at 250 °C for 30 min) was spin-coated to support a thin film metallic electrode layer (e-beam sputtered Au–Cr with a thickness of 150 and 10 nm). Then, photolithography (URE-2000B) and etching processes were applied to form the desired metallic electrodes for the electric circuits. Subsequently, another polyimide layer (2 µm, annealed at 250 °C for 30 min) was spin-coated on the metallic pattern, followed with photolithography and a selective reactive ion

etching process to remove other parts so that only the coated connecting lines of electric circuits were retained. Finally, the thin layer of Au–Cr–PI electrodes was transferred onto the surface of the TC membrane (roughly 300 µm thick).

Assembly of multimodal haptic feedback patch

Commercial TC materials (PINSAl, GK-920, silicon compounds 35%, carbon compounds 35%, metal-oxide compounds 30%) were drop cast on the glass and annealed at 100 °C for 60 min to obtain the smooth TC membrane (Supplementary Fig. 9). TC membranes with designed morphology can be fabricated by polyvinyl acetate modes. The fabrication process of electric circuits started on a thin polydimethylsiloxane layer with a Cu foil (18 µm)-coated polyimide (12.5 µm) layer attached on it. Laser cutting was used to obtain the desired metallic electrode patterns, which can be transferred onto a TC layer with designed morphology, followed by soldering thermoelectric pellets and mechanical actuators on the electrodes (Supplementary Fig. 2). The unique mechanism of the thermoelectric devices required soldering n- and p-type pellets (bismuth telluride, $1.3 \times 1.3 \times 1.65 \text{ mm}^3$) alternately. Each mechanical actuator was close to a pair of thermoelectric pellets in one unit. Subsequently, the surrounding of these pellets and actuators was encompassed with $\text{SiO}_2\text{-Al}_2\text{O}_3$ thermal insulation microfibres (Supplementary Fig. 10), which was prepared by blow spinning following the method reported in ref. 42. The photo-defined Au–Cr–PI electrodes layer were transferred onto another layer of TC membrane with a thin layer of uncured material. After curing, an array of holes was created that are aligned to the position of the actuators. Finally, the thin layer of TC membrane (roughly 300 µm thick) with Au–Cr–PI electrodes was coated on top of the thermoelectric pellets and mechanical actuators.

Control circuits

There are two kinds of control circuit in our system: one is a wireless control circuit that can communicate through BLE and is powered by a battery and the other is a USB connected circuit that communicates through a universal asynchronous receiver and transmitter (Supplementary Fig. 30). The circuit's main parts are as follows: MCU (Supplementary Fig. 31), communication module (universal asynchronous receiver and transmitter or BLE) (Supplementary Fig. 31), voltage conversion module, electrical stimulation module, thermoelectric module and mechanical actuator module. The computer transmits the control signal to the MCU (catalogue no. MSP430F5237 or CC2640R2F, TI) through the communication module (catalogue no. 2450AT18A100E or CH340E, Johanson Technology or WCH). After receiving the command, the MCU controls the electrotactile module, the mechanical actuator module and the thermoelectric module to perform the corresponding actions according to the received commands. The voltage conversion module consists of LDOs, boost converters (Supplementary Fig. 31) and buck converters (Supplementary Fig. 31). LDO (catalogue no. TPS76933, TI) to step down the input voltage to 3.3 V to power the MCU and communication module, while the boost converter module (catalogue nos. LT8364 and LT8331, Analog Devices) steps up the input voltage to 60 V or higher to power the electrotactile module. The power supplies (USB or batteries) can only supply current lower than 1 A. The buck converter (catalogue no. LM3743, TI) is used to step down the input voltage to 2.5 V to increase the output current capability to drive mechanical actuators and thermoelectric modules, thus the maximum output currents can reach 2 A. The electrotactile module contains multiple eight-channel multiplexers (catalogue no. MAX14752, Maxim Integrated) and multiple electrodes in contact with the skin. The MCU controls the activation of electrotactile output channels through the control ports of the multiplexer, thus generating electrotactile signals of different frequencies and duty cycles. The mechanical actuator module uses metal-oxide–semiconductor field-effect transistor (catalogue no. CSD13380F3, TI) as electronic switches, each of which controls a corresponding actuator, and the MCU controls the actuator to vibrate

at different frequencies and intensities by controlling the on/off function of the electronic switches. The thermoelectric module consists of H-bridges (catalogue no. DRV8837, TI) and their corresponding thermoelectric pellets. The MCU can control the corresponding thermoelectric pellets for heating or cooling by controlling the on/off and voltage direction of the H-bridges. The speed of heating or cooling and the final temperature can be controlled by controlling the pulse width modulator's duty cycle.

Characterization

The current and voltage data was measured by data acquisition and multimeter system (catalogue no. DAQ6510, Keithley) with a constant-frequency sampling of 1,000 Hz. The temperature change was measured by k-type thermocouples (Kaipusen) and infrared camera (catalogue no. FLIR A325sc). Scanning electron microscopy images were taken using a field emission scanning electron microscope (catalogue no. LEO-1530). The photographs of vibrating mechanical actuators were taken by a high-speed camera (Photron FASTCAM SA4) at a typical recording speed of 2,000 frames per s. The thermal conductivity coefficient of thermally conductive materials was measured using a DRL-III thermal conductivity coefficient meter. The pressure signals were measured by a piezoelectric pressure sensor (FLEXIFORCE). The accelerator signals were measured by a three-axis accelerometer (ADXL335) in three axes.

VR system

We adapted an Oculus Rift HMD, which is a low-cost and widely used VR device. Oculus Rift was equipped with per-eye displays with high-resolution images of $1,080 \times 1,200$ pixels. Rift has an integrated headset that provides specialized sound effects and has six degrees of freedom rotation and position tracking technology. The Leap Motion Controller is a small USB peripheral device, which can effectively track the position and motion of the human hand in 3D space. At the same time, Leap Motion can also support multiple platforms. The software is written in C# and the VR applications are implemented in the Unity3D game engine. We used Unity3D to integrate all the application components and displayed the created VR application in real-time on Oculus Rift HMD. To provide users with a more immersive experience, we also designed various interactive functions using the Leap Motion Controller. In addition, we used 3D modelling software (such as 3ds Max, Blender and Zbrush) to design and build the props and environments, then imported the built models and animations into the Unity3D engine.

Data availability

The data that support the plots within this paper and other findings of this study are available from the corresponding authors on reasonable request.

Code availability

Custom code used in the study is available from the corresponding authors upon reasonable request.

References

- Keef, C. V. et al. Virtual texture generated using elastomeric conductive block copolymer in a wireless multimodal haptic glove. *Adv. Intell. Syst.* **2**, 2000018 (2020).
- Flesher, S. N. et al. A brain-computer interface that evokes tactile sensations improves robotic arm control. *Science* **372**, 831 (2021).
- Zhu, M. et al. Haptic-feedback smart glove as a creative human-machine interface (HMI) for virtual/augmented reality applications. *Sci. Adv.* **6**, eaaz8693 (2020).
- Steed, A., Friston, S., Pawar, V. & Swapp, D. Docking haptics: extending the reach of haptics by dynamic combinations of grounded and worn devices. In *Proc. 26th ACM Symposium on Virtual Reality Software and Technology Article 2* (ACM, 2020).

5. Ilkhani, G., Aziziaghdam, M. & Samur, E. Data-driven texture rendering on an electrostatic tactile display. *Int. J. Hum. Comput. Interact.* **33**, 756–770 (2017).
6. De Paolis, L. T. & De Luca, V. The impact of the input interface in a virtual environment: the Vive controller and the Myo armband. *Virtual Real.* **24**, 483–502 (2020).
7. Yu, X. et al. Skin-integrated wireless haptic interfaces for virtual and augmented reality. *Nature* **575**, 473–479 (2019).
8. Jung, Y. H., Kim, J.-H. & Rogers, J. A. Skin-integrated vibrohaptic interfaces for virtual and augmented reality. *Adv. Funct. Mater.* **31**, 2008805 (2020).
9. Yang, T.-H. et al. Recent advances and opportunities of active materials for haptic technologies in virtual and augmented reality. *Adv. Funct. Mater.* **31**, 2008831 (2021).
10. Augustine, G. J. et al. The Somatic Sensory System (eds Dale Purves et al.). In *Neuroscience*. Ch. 8, 189–208 (Sinauer Associates, Inc., 2004).
11. Vallbo, A. B. & Johansson, R. S. Properties of cutaneous mechanoreceptors in the human hand related to touch sensation. *Hum. Neurobiol* **3**, 3–14 (1984).
12. Saal, H. P., Delhaye, B. P., Rayhaun, B. C. & Bensmaia, S. J. Simulating tactile signals from the whole hand with millisecond precision. *Proc. Natl Acad. Sci. USA* **114**, E5693 (2017).
13. Jin, H. et al. Highly pixelated, untethered tactile interfaces for an ultra-flexible on-skin telehaptic system. *NPJ Flex. Electron.* **6**, 82 (2022).
14. Yem, V. & Kajimoto, H. Wearable tactile device using mechanical and electrical stimulation for fingertip interaction with virtual world. In *Proc. 2017 IEEE Virtual Reality (VR)* 99–104 (IEEE, 2017).
15. Yin, J., Hincher, R., Shea, H. & Majidi, C. Wearable soft technologies for haptic sensing and feedback. *Adv. Funct. Mater.* **31**, 2007428 (2020).
16. You, I. et al. Artificial multimodal receptors based on ion relaxation dynamics. *Science* **370**, 961–965 (2020).
17. Lee, J., Kim, D., Sul, H. & Ko, S. H. Thermo-haptic materials and devices for wearable virtual and augmented reality. *Adv. Funct. Mater.* **31**, 2007376 (2021).
18. Hong, S. et al. Wearable thermoelectrics for personalized thermoregulation. *Sci. Adv.* **5**, eaaw0536 (2019).
19. Nam, J., Kim, Y. & Jang, G. Resonant piezoelectric vibrator with high displacement at haptic frequency for smart devices. *IEEE ASME Trans. Mechatron.* **21**, 394–401 (2016).
20. Pyo, D., Yang, T.-H., Ryu, S. & Kwon, D.-S. Novel linear impact-resonant actuator for mobile applications. *Sens. Actuator A Phys.* **233**, 460–471 (2015).
21. Jung, Y. H. et al. A wireless haptic interface for programmable patterns of touch across large areas of the skin. *Nat. Electron.* **5**, 374–385 (2022).
22. Delazio, A. et al. Force jacket: pneumatically-actuated jacket for embodied haptic experiences. In *Proc. 2018 CHI Conference on Human Factors in Computing Systems* Paper 320 (Association for Computing Machinery, 2018).
23. Sonar, H. A. & Paik, J. Soft pneumatic actuator skin with piezoelectric sensors for vibrotactile feedback. *Front. Robot. AI* **2**, 38 (2016).
24. Yoshimoto, S., Kuroda, Y., Kagiyama, Y., Kuroda, T. & Oshiro, O. Tactile mapping approach using electrical stimulus pattern. In *Proc. RO-MAN 2009. The 18th IEEE International Symposium on Robot and Human Interactive Communication* 460–465 (IEEE, 2009).
25. Chun, S. et al. An artificial neural tactile sensing system. *Nat. Electron.* **4**, 429–438 (2021).
26. Tsai, D. R. & Hsu, W. A new type of a large-area multi-touch tactile device operated by electrotactile stimulation. In *Proc. 2019 IEEE World Haptics Conference (WHC)* 313–318 (IEEE, 2019).
27. Yao, K. et al. Encoding of tactile information in hand via skin-integrated wireless haptic interface. *Nat. Mach. Intell.* **4**, 893–903 (2022).
28. Kajimoto, H., Kawakami, N. & Tachi, S. Psychophysical evaluation of receptor selectivity in electro-tactile display. In *Proc. of 13th International Symposium on Measurement and Control in Robotics (ISMCR)*. 13, 83–86 (IEEE, 2003).
29. Kaczmarek, K. A., Webster, J. G., Bach-y-Rita, P. & Tompkins, W. J. Electrotactile and vibrotactile displays for sensory substitution systems. *IEEE Trans. Biomed. Eng.* **38**, 1–16 (1991).
30. Shi, Y. et al. Self-powered electro-tactile system for virtual tactile experiences. *Sci. Adv.* **7**, eabe2943 (2021).
31. Xu, B. et al. An epidermal stimulation and sensing platform for sensorimotor prosthetic control, management of lower back exertion, and electrical muscle activation. *Adv. Mater.* **28**, 4462–4471 (2016).
32. Zárate, J. J., Tosolini, G., Petroni, S., De Vittorio, M. & Shea, H. Optimization of the force and power consumption of a microfabricated magnetic actuator. *Sens. Actuator A Phys.* **234**, 57–64 (2015).
33. Li, D. et al. Miniaturization of mechanical actuators in skin-integrated electronics for haptic interfaces. *Microsyst. Nanoeng.* **7**, 85 (2021).
34. Huang, Y. et al. Recent advances in multi-mode haptic feedback technologies towards wearable interfaces. *Mater. Today Phys.* **22**, 100602 (2021).
35. Yem, V. & Kajimoto, H. Comparative evaluation of tactile sensation by electrical and mechanical stimulation. *IEEE Trans. Haptics* **10**, 130–134 (2016).
36. Yang, Y., Zhou, Y., Zeng, J., He, K. & Liu, H. Electrotactile stimulation waveform modulation based on a customized portable stimulator: a pilot study. In *Proc. 2019 IEEE International Conference on Systems, Man and Cybernetics (SMC)* 1838–1843 (IEEE, 2019).
37. Kajimoto, H., Kawakami, N., Maeda, T., Tachi, S. Electro-tactile display with tactile primary color approach. In *Proceedings of the 2004 IEEE/RSJ International Conference on Intelligent Robots and Systems* Vol. 2, 541–546 (IEEE, 2004).
38. Kenshalo, D. R., Holmes, C. E. & Wood, P. B. Warm and cool thresholds as a function of rate of stimulus temperature change. *Percept. Psychophys.* **3**, 81–84 (1968).
39. Konyo, M., Tadokoro, S., Yoshida, A. & Saiwaki, N. A tactile synthesis method using multiple frequency vibrations for representing virtual touch. In *Proc. 2005 IEEE/RSJ International Conference on Intelligent Robots and Systems* 3965–3971 (IEEE, 2005).
40. Culbertson, H., Unwin, J. & Kuchenbecker, K. J. Modeling and rendering realistic textures from unconstrained tool-surface interactions. *IEEE Trans. Haptics* **7**, 381–393 (2014).
41. Okamoto, S., Nagano, H. & Yamada, Y. Psychophysical dimensions of tactile perception of textures. *IEEE Trans. Haptics* **6**, 81–93 (2013).
42. Jia, C. et al. Highly compressible and anisotropic lamellar ceramic sponges with superior thermal insulation and acoustic absorption performances. *Nat. Commun.* **11**, 3732 (2020).

Acknowledgements

This work was supported by Research Grants Council of the Hong Kong Special Administrative Region (grant nos. 11215722, 11213721 and 11211523), City University of Hong Kong (grant nos. 9667221 and 9680322), National Natural Science Foundation of China (grant nos. 62122002, 12072057, 62172346 and 61907037), Shenzhen Science and Technology Innovation Commission (grant nos. SGDX2022053011401011 and JCYJ20200109110201713) and the Innovation and Technology Fund of Innovation and Technology Commission (grant no. GHP/095/20GD), as part of the InnoHK Project on Project 2.2—AI-based 3D ultrasound imaging algorithm at Hong Kong Centre for Cerebro-Cardiovascular Health Engineering,

Guangdong Basic and Applied Basic Research Foundation (project no. 2021A1515011893) and the Centre for Applied Computing and Interactive Media of School of Creative Media, City University of Hong Kong; The CityU Contract Research RMGS (project no. 9239092), the CityU Donations for Research Projects RMGS (project no. 9229075); LiaoNing Revitalization Talents Programme (grant no. XLYC2007196) and the Dalian Outstanding Young Talents in Science and Technology (grant no. 2021RJ06). E.S. acknowledges support from the Shanghai Municipal Science and Technology Major Project (no. 2018SHZDZX01), the ZJ Laboratory and Shanghai Centre for Brain Science and Brain-Inspired Technology.

Author contributions

X.Y. and Y.H. initiated the concept and proposed the project. Y.H. designed the whole system and collected the overall data. Y.H., J.Z., X.Y., Z.X. and Mr. X.G optimized the structure of feedback device. J.Z and Y.H. designed and characterized control circuits. Y.H., C.K.Y., D.L., K.Y., Y.G., Z.C. and Jiyu Li fabricated the feedback devices. P.K. and Y.H. set up the VR scenes. Y.H., J.Z., P.K., K.Z. and S.C. designed and organized user studies. Y.H., X.Y., S.C., P.K., K.Z. and K.Y. analysed the data obtained from user studies. X.G. and Z.X. led the mechanical, thermal, and electrical modelling and related finite element analysis. Prof. X.G. gave comments on mechanical modelling. Y.H., J.Z., P.K., S.C., Mr. X.G., Z.X., K.Z. and X.Y. wrote the manuscript. All other authors contributed to discussing the data and commenting on the final manuscript.

Competing interests

The authors declare no competing interests.

Additional information

Extended data is available for this paper at <https://doi.org/10.1038/s41928-023-01074-z>.

Supplementary information The online version contains supplementary material available at <https://doi.org/10.1038/s41928-023-01074-z>.

Correspondence and requests for materials should be addressed to Zhaoqian Xie, Kening Zhu or Xinge Yu.

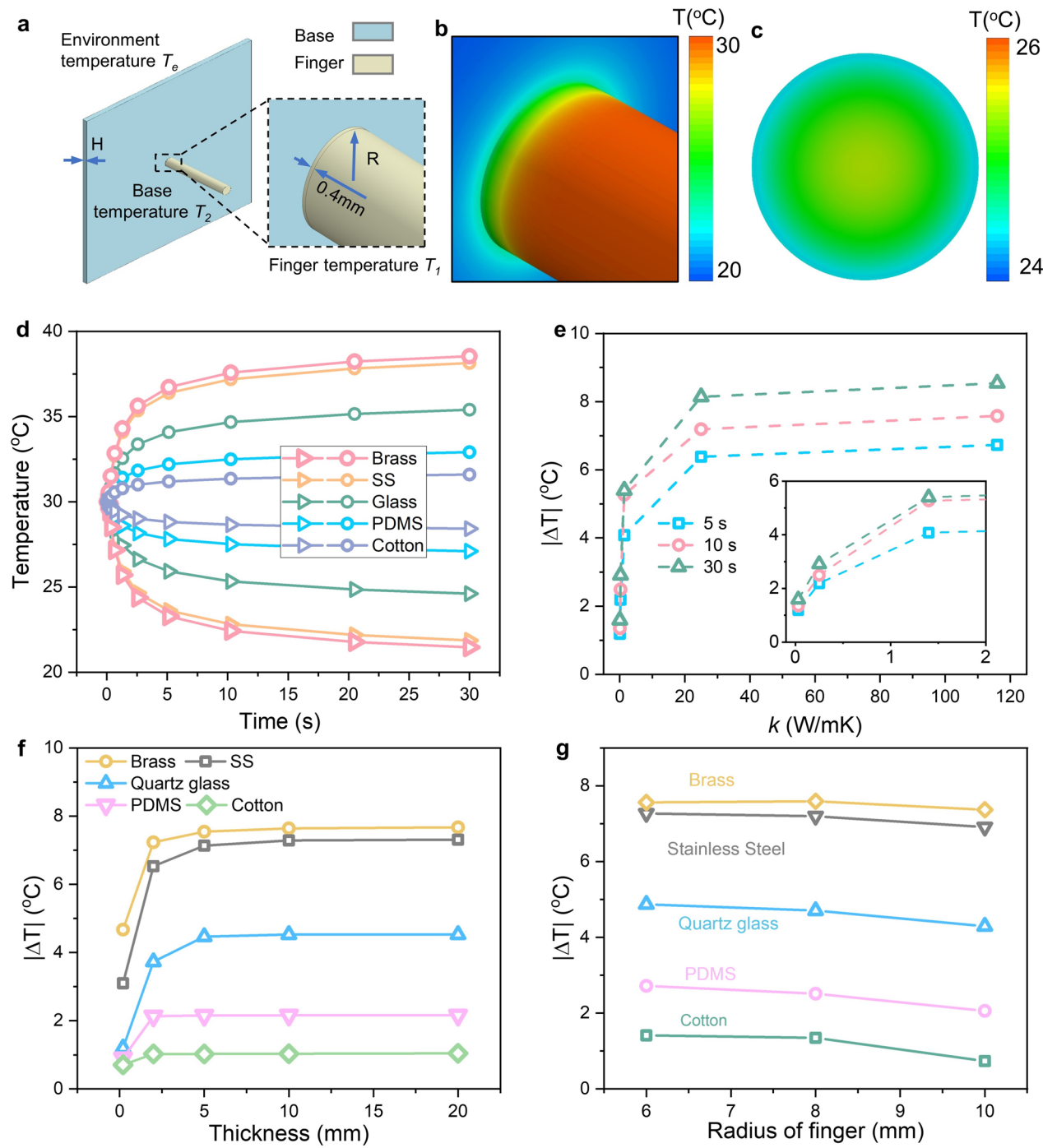
Peer review information *Nature Electronics* thanks Hye Jin Kim, Fang Yi and the other, anonymous, reviewer(s) for their contribution to the peer review of this work.

Reprints and permissions information is available at www.nature.com/reprints.

Publisher's note Springer Nature remains neutral with regard to jurisdictional claims in published maps and institutional affiliations.

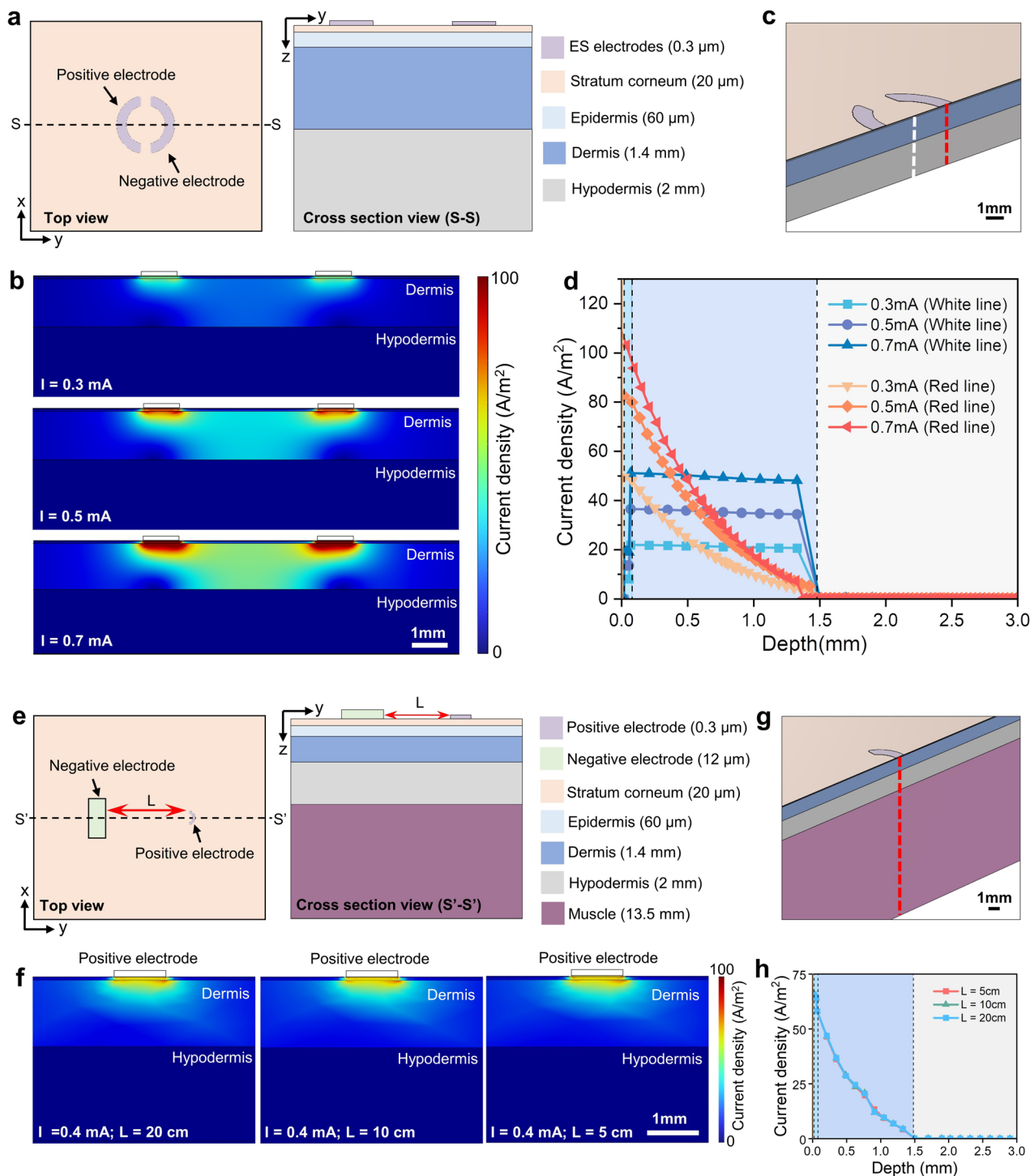
Springer Nature or its licensor (e.g. a society or other partner) holds exclusive rights to this article under a publishing agreement with the author(s) or other rightsholder(s); author self-archiving of the accepted manuscript version of this article is solely governed by the terms of such publishing agreement and applicable law.

© The Author(s), under exclusive licence to Springer Nature Limited 2023, corrected publication 2023



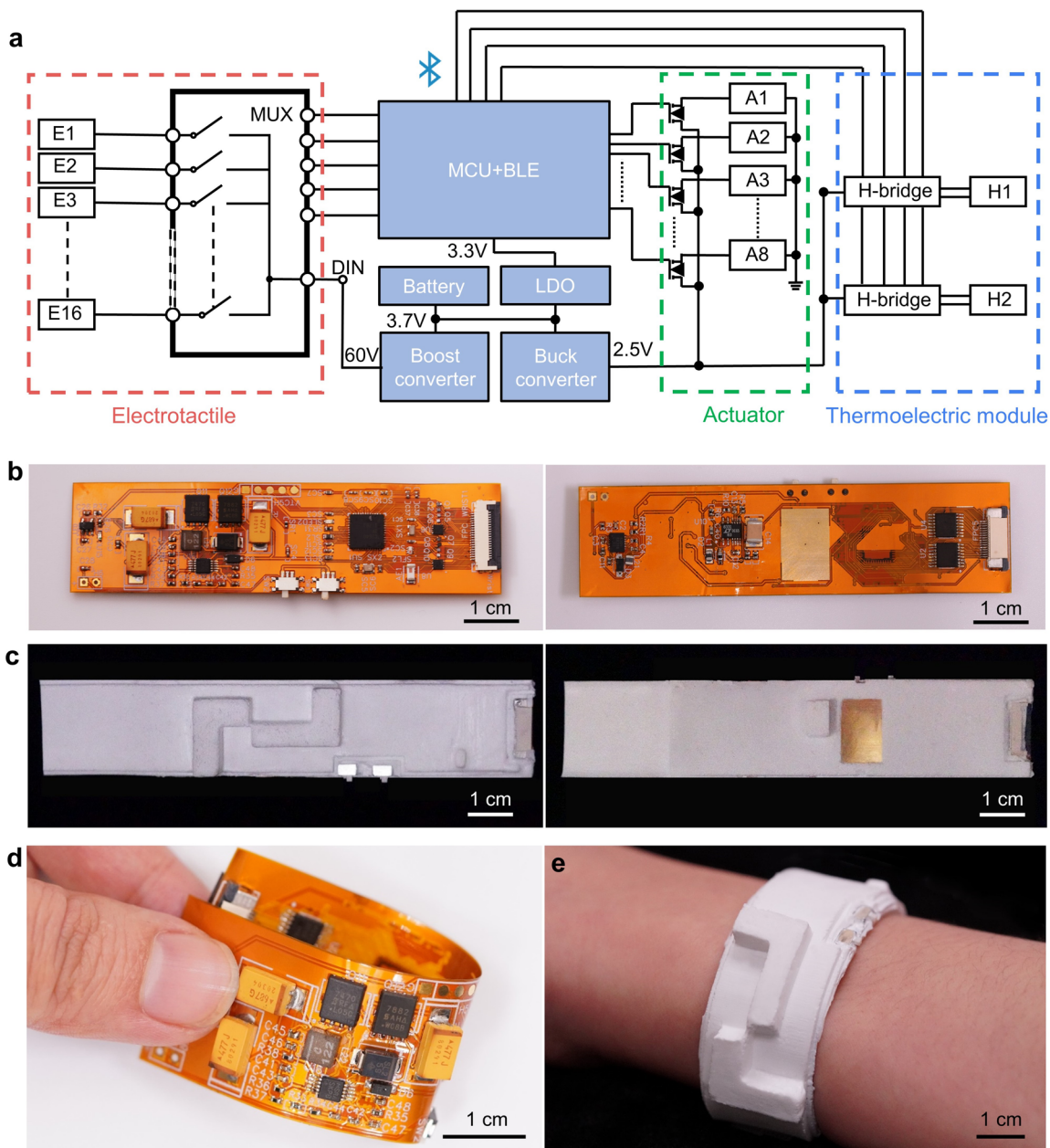
Extended Data Fig. 1 | Thermal simulation of the temperature changes when finger touch different materials. **a**, The schematic diagram of the thermal simulation model where the finger is simplified into a cylinder. The thermoreceptors are set at a depth of 0.4 mm under the skin. The temperature distribution around the contact region (**b**) and the thermoreceptors (**c**) for the finger ($R = 8\text{ mm}$) touching a 5 mm thick quartz glass base at 30 s, in which $T_f = 30\text{ °C}$, $T_2 = T_e = 20\text{ °C}$, $L = 70\text{ mm}$. **d**, Time-dependent temperature change

curves when a finger (6 mm radius, 30 °C) touches a 2 cm-thick base with different materials (20 °C). **e**, Summary of the temperature changes in (**d**) at 5 s, 10 s and 30 s after touching. **f**, The average temperature changes (over the thermoreceptors) of a finger with 8 mm radius touching the base with different materials and thicknesses at 10 s. **g**, The average temperature changes (over the thermoreceptors) for the fingers with different radii touching a 5 mm-thick base with different materials at 10 s.

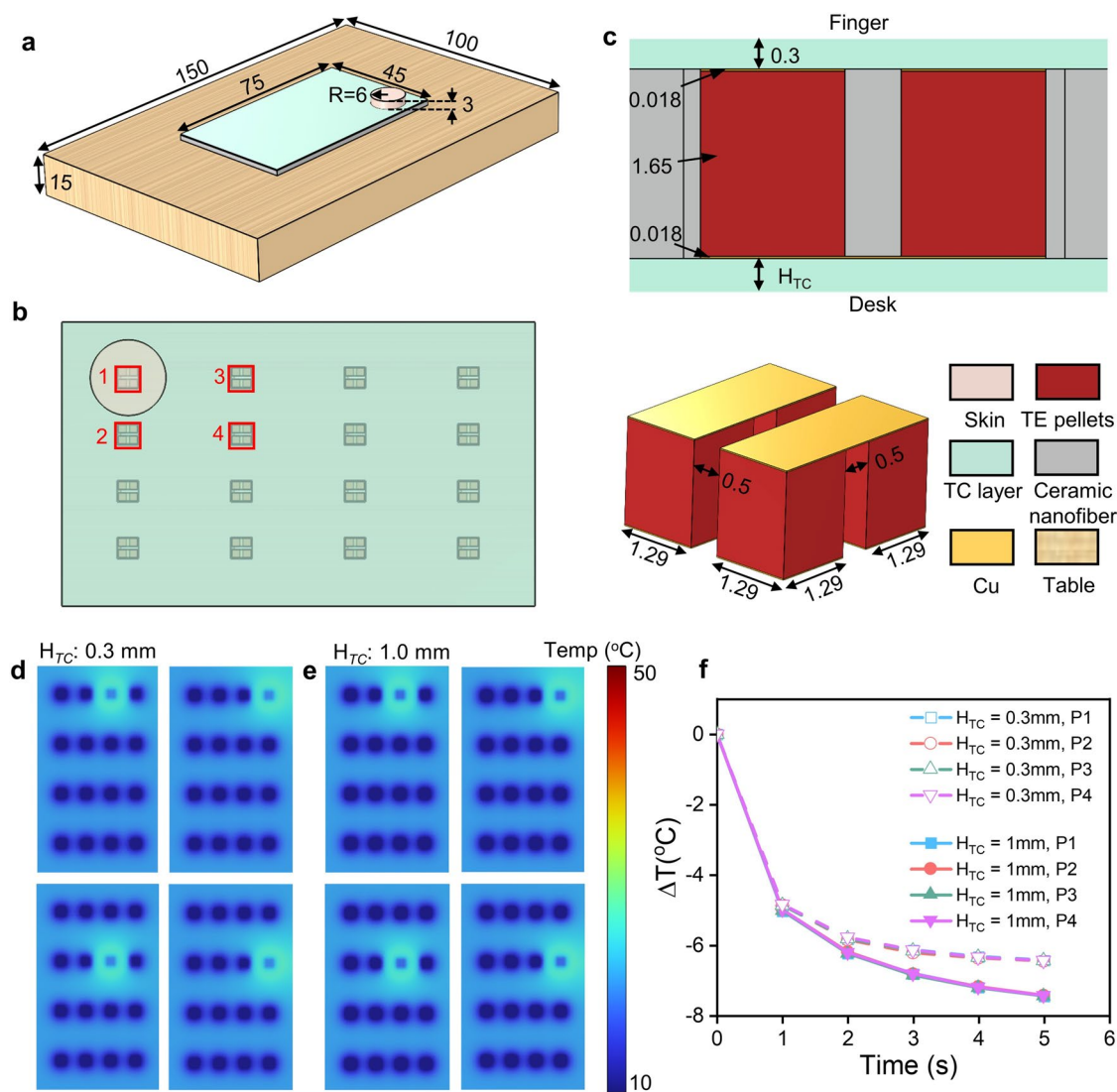


Extended Data Fig. 2 | The simulation models for electrotactile. **a**, Schematic diagram of the electrode geometries and the tissue layers used in simulation using two circular electrode. **b**, The distribution of current density around two electrodes with different currents values. **c**, Two positions chosen for analysis of current density distribution, directly under the electrode (red line) and in the middle of two electrodes (white line). **d**, The current density changes versus depth under the electrode and in the middle of two electrodes. **e**, Schematic

diagram of the electrode geometries and the tissue layers used in simulation using a circular positive electrode and a rectangular negative electrode. **f**, The distribution of current density under the circular electrode with different distance L between positive and negative electrodes. **g**, One position directly under the ring electrode (red line) chosen for analysis of current density distribution. **h**, The current density changes versus depth under the electrode.

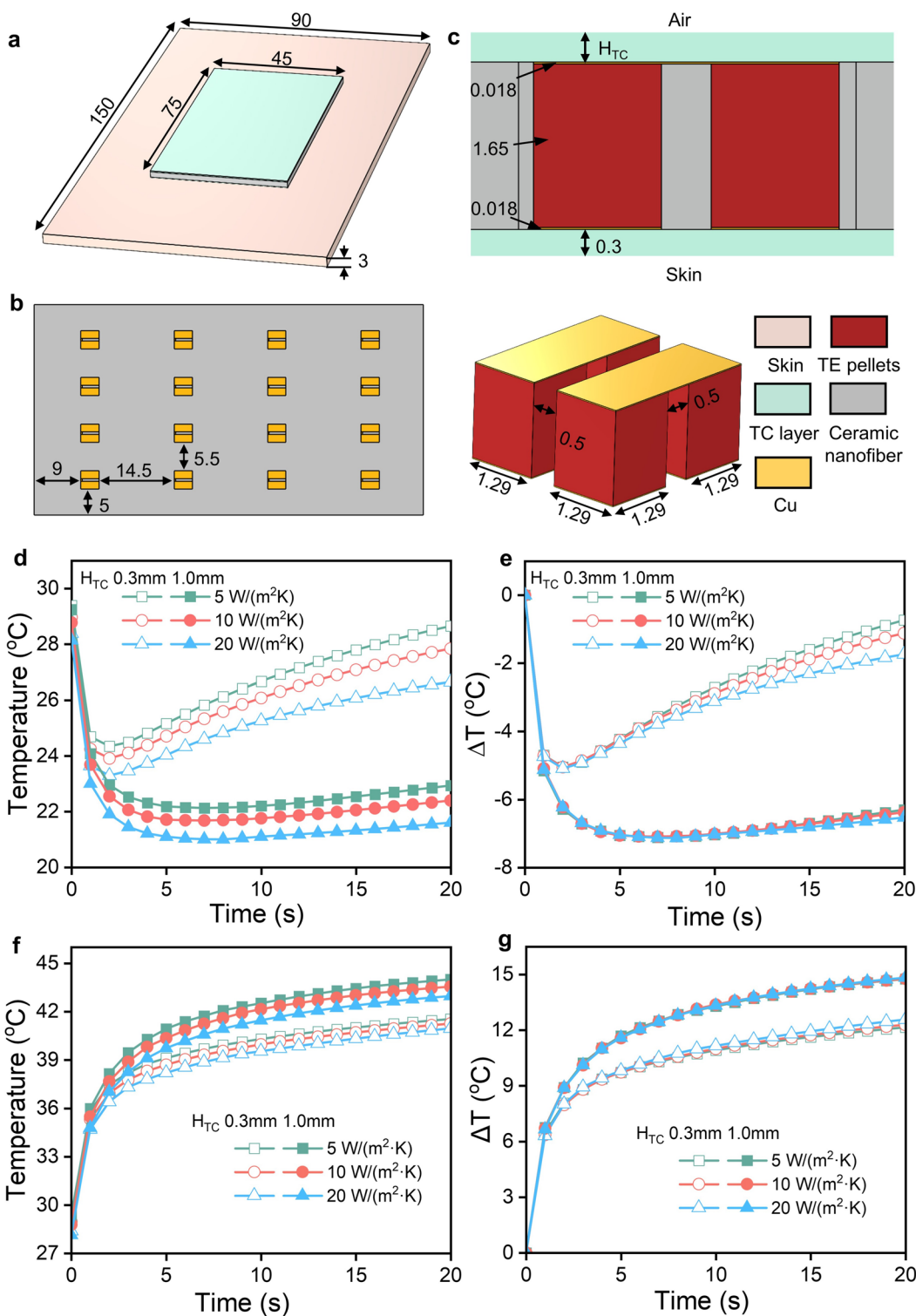


Extended Data Fig. 3 | The wireless control circuits. **a**, Circuit diagram of the wireless control circuits. Photograph of the bare control circuits (both front-view and back-view) (**b**) and encapsulated control circuits (both front-view and back-view) (**c**) as a wristband. The photo of (**d**) the bended circuits and (**e**) the encapsulated wristband worn on the arm.



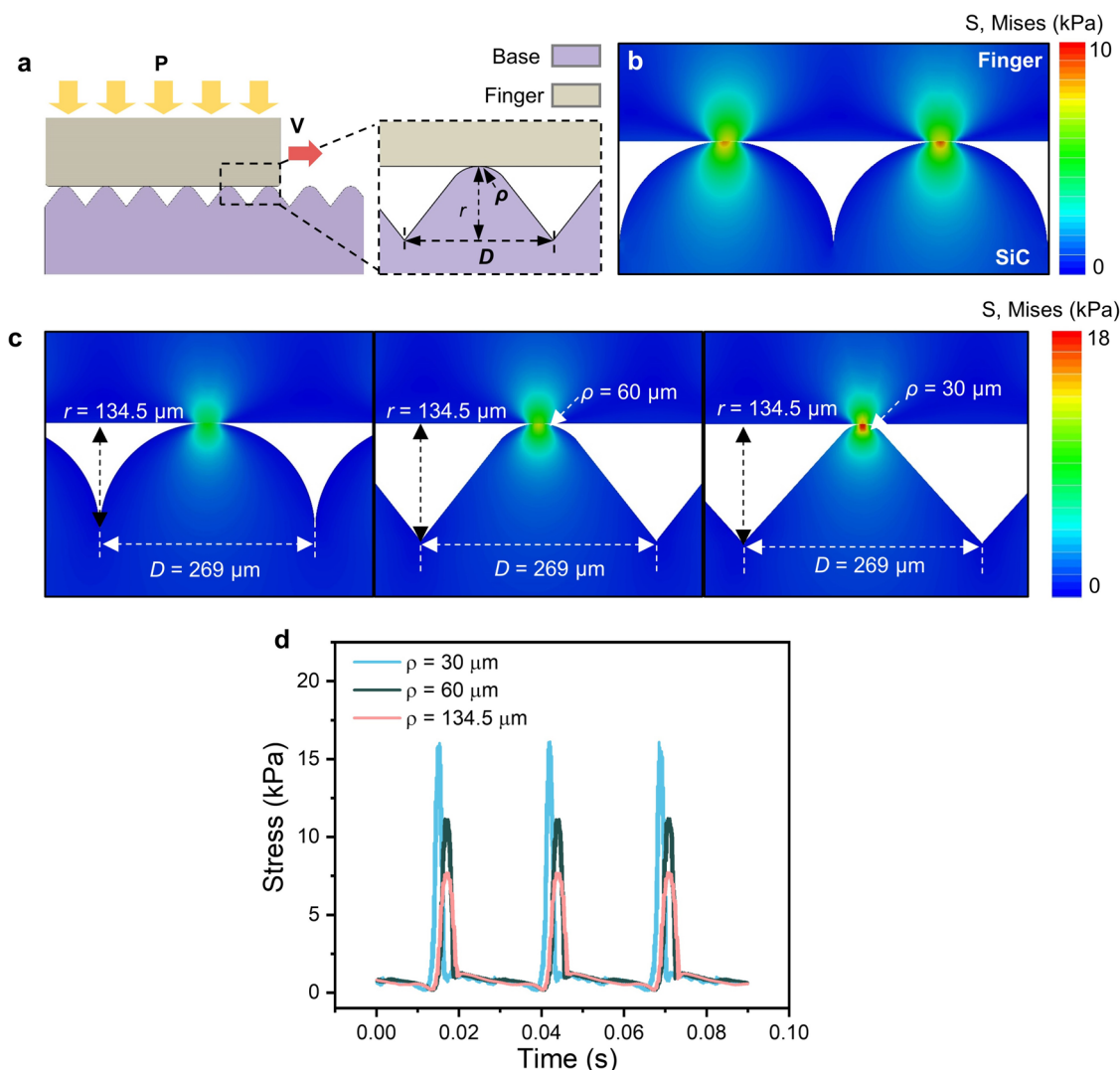
Extended Data Fig. 4 | Influence of the contact positions between the skin and device on the interface temperature. **a**, The schematic diagram of the thermoelectric simulation model. **b**, The four contact positions (P1, P2, P3 and P4) between skin and the device. **c**, The cross section and geometrical dimensions

of the device. The temperature distributions on the contact surface when the skin touches four positions with $H_{TC} = 0.3$ mm (**d**) and $H_{TC} = 1.0$ mm (**e**) (1 A, 20 s), respectively. **f**, The average temperature change over each contact position versus time. The unit of number in this figure is mm.



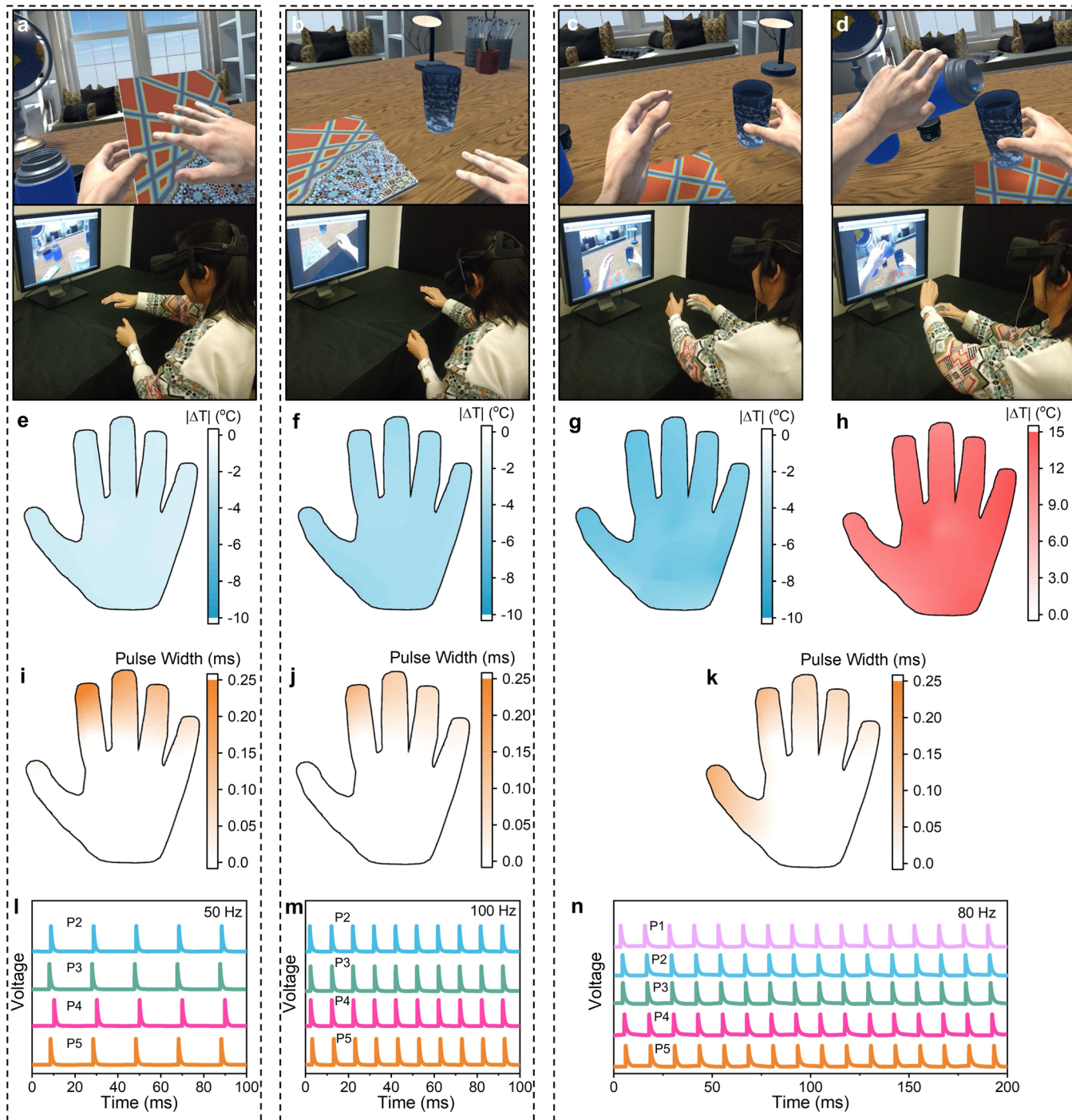
Extended Data Fig. 5 | Simulation model of heat dissipation capability for the device mounted on skin. **a**, Schematic diagram for the device attached on skin. **b**, The geometric dimensions and **c**, cross section of the thermoelectric part. **d**, The absolute average temperature and **e**, the relative average temperature of the surface contacted with skin at the position 4 with the input current 1 A in the cooling mode, respectively. **f**, The absolute average temperature and **g**, the relative average temperature of the surface contacted with skin at the position 4 with the input current 1 A in the heating mode, respectively. The unit of number in this figure is mm.

the cooling mode, respectively. **f**, The absolute average temperature and **g**, the relative average temperature of the surface contacted with skin at the position 4 with the input current 1 A in the cooling mode, respectively. The unit of number in this figure is mm.



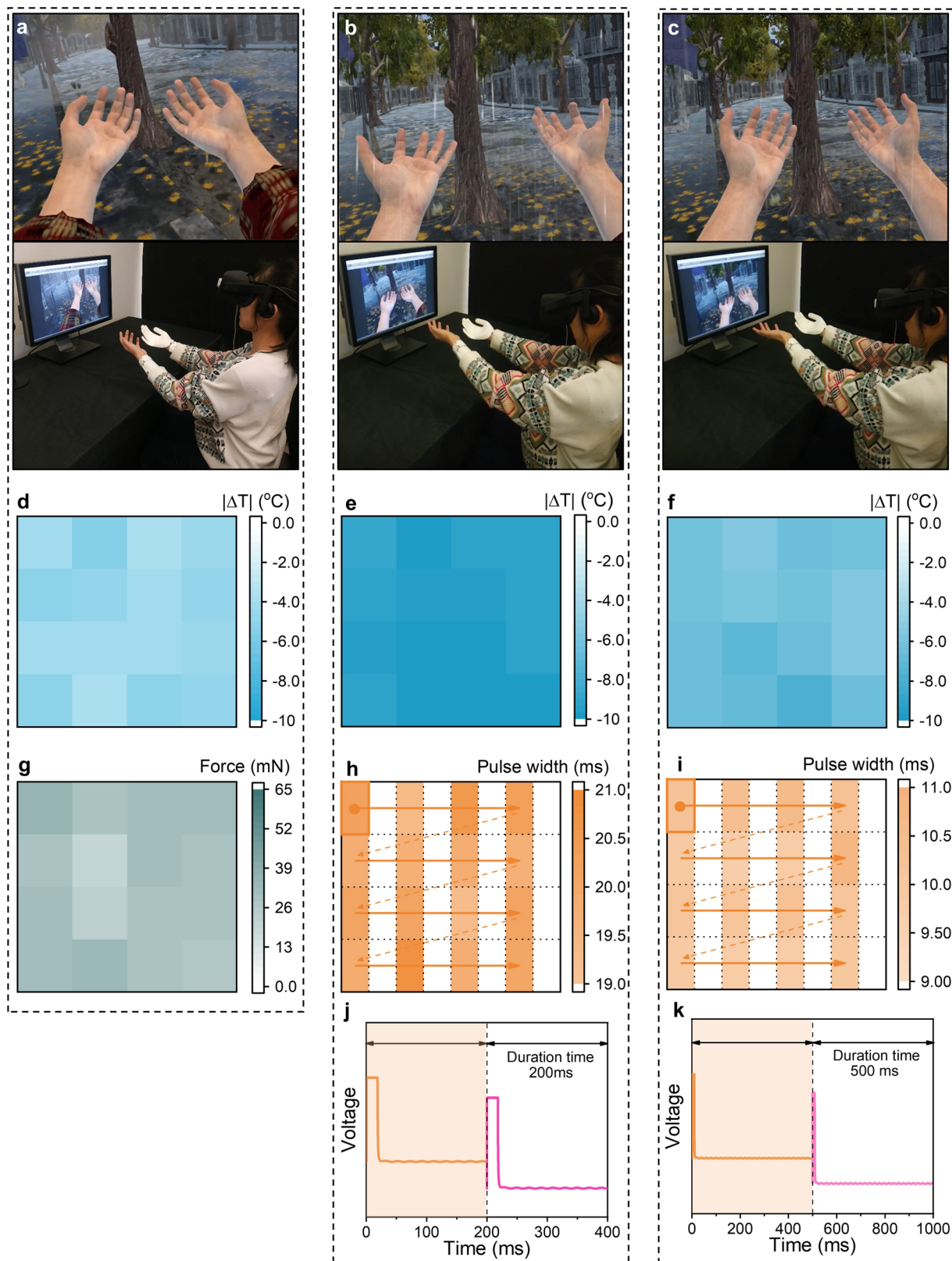
Extended Data Fig. 6 | Roughness simulation related with the desired surface and the finger speed. **a**, The schematic diagram of the roughness simulation where finger processed on the desired surface with speed of v . **b**, The Von Mises Stress distribution when finger pressed on the surface composed of semi-circular SiCbulge ($d = 269 \mu\text{m}$) with pressure of 1kPa and sliding speed of 1cm/s.

c, The finger presses on three surfaces which composed of bulge of different curvature radius but has the same roughness with pressure of 1kPa and moving velocity of 1 cm/s. **d**, Stress curves of the finger feel when moving on three surfaces with same roughness but different morphology.



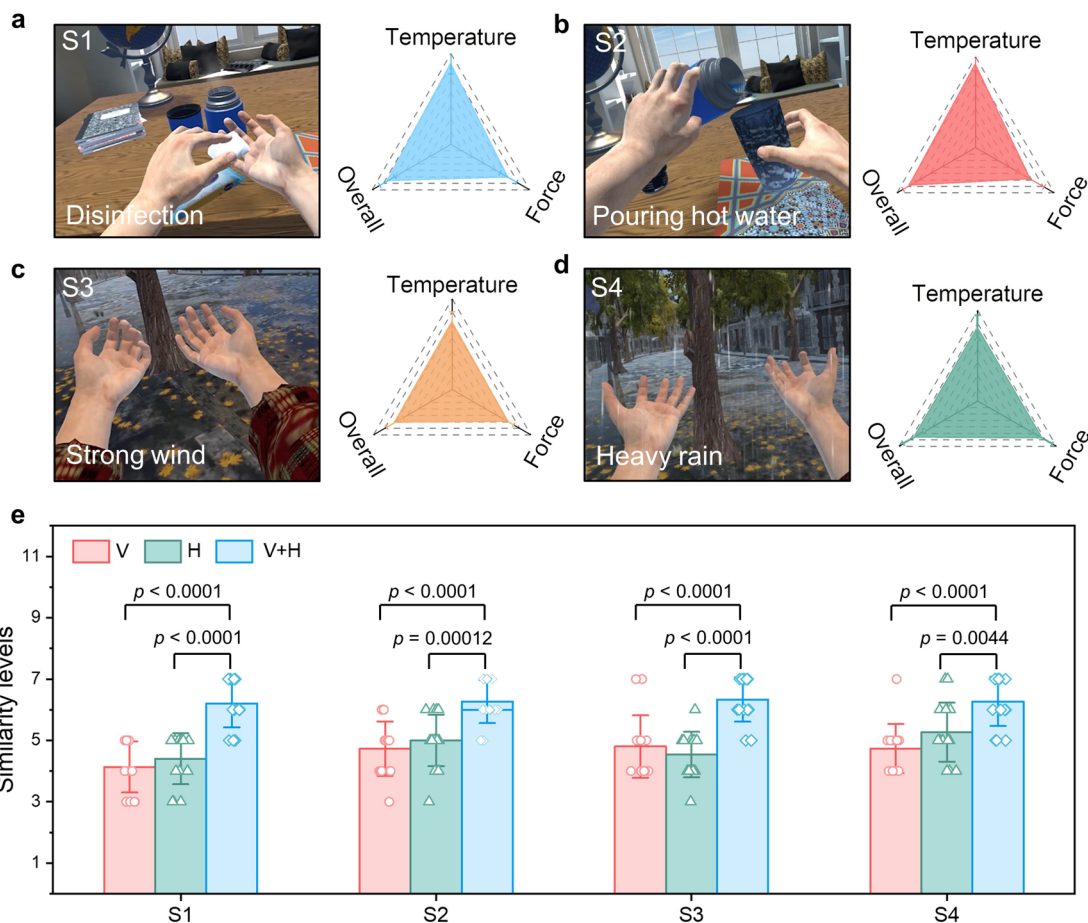
Extended Data Fig. 7 | The VR indoor scenes. The VR scene and actual scene of users touching the cover of a book (a), touching the wood desk (b), holding a glass cup (c) and pouring hot water in the glass cup (d). The temperature change of touching the book is set around -2°C (e), touching the desk is set around -4°C (f) and touching the glass bottle is set around -6°C (g) in virtual world due to the simulation results and pre-user tests. The temperature first decreases due to the lower temperature of the bottle, but the temperature raises drastically ($+12^{\circ}\text{C}$) once hot water is poured into the bottle (h). The mechanical stimulus obtained

from sliding on the book is mainly fine roughness, and the mechanical stimulus obtained from the book is mainly the hardness, thus the pulse width of touching book (i) is higher than that of touching the desk (j) and the frequency of touching desk (m) is much higher than that of touching the book (l) for getting a pulse-undistinguished pressure. For holding the bottle, five fingers are pressed on the virtual object (k) and the electrotactile activated when holding the bottle is a feeling composed of vibration and pressure reported by the users (n).



Extended Data Fig. 8 | The VR outdoor scenes. The VR scene and actual scene of users experiencing light breeze (a), heavy rain (b), and light rain with her arm (c). The heavy rain leads to an obvious temperature decrease (e) than light breeze (d) and light rain (f). The breeze blows up the sleeves and the arm feel slight force (g).

Raindrops drop on the arm and cause impacts on the arm. Due to the randomness of the location of the fall, the activated electrodes are always changing (h) (i). And the stimulation pulse of heavy rain (j) is set stronger and denser compared with that of light rain (k).



Extended Data Fig. 9 | The similarity ratings of four virtual scenes. The photograph of four scenes, **a**, S1: disinfections with 75% alcohol tissue, **b**, S2: pouring hot water into a glass bottle, **c**, S3: strong wind and **d**, S4: heavy rain, and corresponding average similarity levels in temperature, force and overall obtained from user study. **e**, Statistic histograms of similarity levels when users

only got visual and auditory signals, only got haptic feedback, or got all visual, auditory signals and haptic feedback. Center line, median; bar height, mean; error bars, SD; n = 15 independent tests. Statistical significance was assessed using two-sided unpaired *t*-tests.